

Resource-efficient quantum simulation of transport phenomena via Hamiltonian embedding

Joseph Li,^{1,2} Gengzhi Yang,^{2,3} Jiaqi Leng,^{4,5} and Xiaodi Wu^{1,2,*}

¹*Department of Computer Science, University of Maryland, College Park, Maryland 20742, USA*

²*Joint Center for Quantum Information and Computer Science,
University of Maryland, College Park, Maryland 20742, USA*

³*Department of Mathematics, University of Maryland, College Park, Maryland 20742, USA*

⁴*Simons Institute for the Theory of Computing, UC Berkeley, California 94709, USA*

⁵*Department of Mathematics, UC Berkeley, Berkeley, California 94709, USA*

(Dated: February 4, 2026)

Transport phenomena play a key role in a variety of application domains, and efficient simulation of these dynamics remains an outstanding challenge. While quantum computers offer potential for significant speedups, existing algorithms either lack rigorous theoretical guarantees or demand substantial quantum resources, preventing scalable and efficient validation on realistic quantum hardware. To address this gap, we develop a comprehensive framework for simulating classes of transport equations, offering both rigorous theoretical guarantees—including exponential speedups in specific cases—and a systematic, hardware-efficient implementation. Central to our approach is the Hamiltonian embedding technique, a white-box approach for end-to-end simulation of sparse Hamiltonians that avoids abstract query models and retains near-optimal asymptotic complexity. Empirical resource estimates indicate that our approach can yield an order-of-magnitude (e.g., $42\times$) reduction in circuit depth given favorable problem structures. We then apply our framework to solve linear and nonlinear transport PDEs, including the first experimental demonstration of a 2D advection equation on a trapped-ion quantum computer.

I. INTRODUCTION

Transport phenomena are fundamental to understanding processes across all scales in nature, serving as a cornerstone in the study of fluid dynamics [1, 2], chemical reactions [3, 4], and thermodynamics [5]. Partial differential equations (PDEs) are central to the modeling of transport dynamics. While numerical solutions to these models are often desired to facilitate scientific investigation or engineering design, they are largely limited to low-dimensional settings, as computational cost typically scales exponentially with model dimension. This makes accurate modeling of high-dimensional transport phenomena, such as those in phase space [6], parameter space [7], or multi-species chemical diffusion [8], prohibitively expensive for traditional approaches.

Quantum computing has provided an alternative yet potentially promising paradigm for simulating large-scale dynamics, including inherently quantum phenomena [9] and complex classical processes [10, 11]. Given that transport dynamics typically involve a large number of degrees of freedom and exhibit wave-like behaviors, quantum simulation of such phenomena has become an active area of extensive study [12–16].

Existing quantum algorithms for simulating PDEs mainly fall into two categories. The first approach adopts variational quantum algorithms (VQAs) to prepare quantum states that represent solutions to differential equations [17–22]. While these methods are resource-efficient

and have been demonstrated in real quantum hardware, they often fail to offer theoretical guarantees, leaving their scalability in practical problems unclear. The second approach is based on quantum subroutines implemented on fault-tolerant quantum computers, such as Quantum Linear System Solvers (QLSS) [11, 23–25] and Hamiltonian simulation [12, 13, 26–30]. For certain structured dynamical simulations, these quantum algorithms can achieve provable (sometimes exponential) quantum speedups over classical algorithms. Nevertheless, realizing these advantages on near- and intermediate-term quantum hardware remains challenging, even for low-dimensional linear PDEs. A central bottleneck is the quantum input model: one must construct coherent circuits that encode the problem data (e.g., PDE coefficients). Existing approaches, such as sparse-input oracles [31], block-encodings [32], and QRAM [33], are often prohibitively costly and well beyond the capabilities of current quantum devices.

Recently, a new technique called Hamiltonian embedding [34] was proposed to mitigate the significant overhead incurred by sophisticated quantum input models, particularly in sparse Hamiltonian simulation. In this case, the goal is to implement the unitary e^{-itA} for a sparse Hermitian matrix A over an evolution time t . Existing algorithms are often *complexity-theoretically* efficient in the sense that they achieve high-accuracy simulation using only a polynomial number of black-box (oracle) queries to the matrix entries. However, the cost of implementing these oracles is often left implicit without careful analysis. Hamiltonian embedding instead adopts a *white-box* approach. It explicitly maps the target sparse Hamiltonian A into a larger qubit Hamiltonian (the *em-*

* xiaodiwu@umd.edu

(embedding Hamiltonian) composed solely of local Pauli operators. This resulting Hamiltonian can then be efficiently simulated on either digital or analog hardware. For structured families of sparse Hamiltonians, the embedding Hamiltonian can be realized using n qubits and at most n^2 2-qubit interactions, where n is logarithmically small in the size of A , paving a pathway towards an exponential quantum advantage.

In this paper, we develop a framework for resource-efficient quantum simulation of transport dynamics by incorporating Hamiltonian embedding into quantum PDE solvers. Our framework offers three key advantages. (1) Rigorous performance guarantees: for certain classes of transport equations, we prove that our algorithms achieve exponential quantum speedups when implemented on fault-tolerant devices. (2) Hardware-aware compilation: the Hamiltonian embedding can be customized to the native operations supported by the target platform, enabling direct compilation down to the gate or even the pulse level. As a byproduct, we provide resource estimation in terms of gate count and circuit depth for various classes of PDEs and identify the most efficient implementation based on problem structures. (3) Real-machine validation: we implement our approach to simulate a two-dimensional advection equation on a trapped-ion quantum computer (IonQ Aria-1); to the best of our knowledge, this is the first real-hardware demonstration of its kind in the literature [13, 19, 30, 35].

Our framework consists of two major steps, as illustrated in Fig. 1. First, since most transport PDEs are non-unitary processes, they need to be mapped to quantum evolution processes before they can be solved via quantum simulation. In this work, we adopt the Schrödingerization technique [36]. Note that an additional linearization step is necessary for transport dynamics governed by nonlinear PDEs; see the discussion in Sec. V. Second, with spatial discretization, the Schrödingerized transport PDEs are reduced to sparse Hamiltonian simulation problems, which are implemented using quantum circuits via Hamiltonian embedding [34].

Theoretically, we establish the exponential quantum speedup of our framework for PDEs whose spatial discretization admits a sparse, tensor product structure. This problem class encompasses classically intractable problems, such as the spatially varying advection equation and nonlinear scalar hyperbolic PDEs. Our framework mainly relies on Algorithm 1, a quantum ODE solver that integrates Hamiltonian embedding with Schrödingerization and Richardson extrapolation. When applied to transport PDEs in d spatial dimensions, our algorithm uses $\mathcal{O}(d)$ qubits and has gate complexity polynomial in d , indicative of an exponential speedup over classical mesh-based algorithms. More details of the algorithm, including the near-optimal parameter dependence in the evolution time and simulation error, are available in Theorem 1.

We showcase our framework to two fundamental

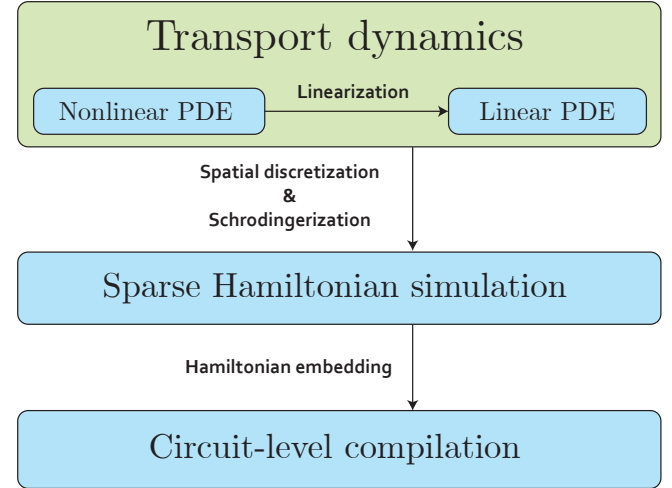


FIG. 1. Schematic of quantum PDE solvers via Hamiltonian embedding.

classes of transport PDEs, including linear advection equations (Sec. IV) and nonlinear scalar hyperbolic equations (Sec. V). These equations are ubiquitous in atmospheric and environmental sciences [3, 37], and form the foundation for more sophisticated models in fluid dynamics [38]. In both cases, we discuss their implementation on quantum computers and conduct extensive resource analyses. For linear advection equations, when incorporating gate-level parallelization, our Hamiltonian embedding approach (using the one-hot embedding) results in the shallowest circuits. For nonlinear scalar hyperbolic PDE, we find that unary and one-hot embeddings outperform the standard binary encoding in both circuit depth and two-qubit gate counts by roughly an order of magnitude.

The paper is structured as follows. In Sec. II, we provide the necessary background on Hamiltonian-simulation-based quantum PDE solvers and introduce the Hamiltonian embedding technique. We also briefly review existing results on real-machine demonstration of PDE simulations and their limitations. In Sec. III, we develop the general framework of simulating transport PDEs via Hamiltonian embedding, with a complexity analysis on the asymptotic gate counts. In Sec. IV and Sec. V, we apply our quantum algorithms to linear advection equations and nonlinear hyperbolic PDEs, respectively. For each model of transport dynamics, we construct its corresponding embedding Hamiltonian, perform numerical simulations, and conduct a resource analysis based on the actual gate counts. We also demonstrate the simulation of a 2D advection equation using the IonQ Aria-1 processor. We conclude in Sec. VI with a discussion.

II. BACKGROUND

A. Schrödingerization

Schrödingerization is a technique that transforms linear, non-unitary dynamics to a unitary PDE described by a Schrödinger equation. Consider a time-evolving linear PDE in d spatial dimensions. To apply Schrödingerization, one discretizes in space to obtain a linear ODE:

$$\frac{du(t)}{dt} = Au(t), \quad u(0) = u_0, \quad (1)$$

where $A \in \mathbb{C}^{N^d \times N^d}$, $u(t) \in \mathbb{C}^{N^d}$, and N is the number of grid points along each dimension. The structure of A depends on the PDE of interest and the spatial discretization scheme; with finite differences, A is generally sparse. Throughout, we express A in terms of its Cartesian decomposition $A = H_1 + iH_2$, where $H_1 = \frac{A+A^\dagger}{2}$ and $H_2 = \frac{A-A^\dagger}{2i}$ are both Hermitian. For stability, H_1 is assumed to be negative semidefinite. Note that this assumption is merely a technical one and can always be satisfied by introducing a global decay rate.

For many interesting PDEs, the real part H_1 is non-zero, leading to a non-unitary dynamics. Schrödingerization leverages the warped phase transformation [27]: $u(t) \mapsto v(t, p) = e^{-p}u(t)$ (where $p > 0$ is an auxiliary variable), which maps the non-unitary dynamics to a Schrödinger-type equation:

$$\begin{aligned} \frac{\partial}{\partial t}v(t, p) &= -H_1 \frac{\partial}{\partial p}v(t, p) + iH_2v(t, p) \\ v(0, p) &= e^{-|p|}u_0. \end{aligned} \quad (2)$$

By using a Hamiltonian simulation algorithm such as [39], the gate complexity of Schrödingerization was shown to be $\tilde{\mathcal{O}}(T/\epsilon)$, assuming the discretization step size for p is chosen as $\Delta p \sim \epsilon$.

It is worth noting that another closely related framework, namely, the linear combination of Hamiltonian simulation (LCHS) [28], may also be used to map non-unitary processes to Hamiltonian evolution. For near-term implementation, the hybrid implementation of LCHS requires the execution of many randomly chosen circuits due to an importance sampling procedure. With the same total number of circuit executions, we find that both methods achieve similar performance (see Appendix G). In this work, we focus on Schrödingerization since it only requires a single quantum circuit.

B. Hamiltonian embedding

Hamiltonian embedding reduces the problem of simulating a sparse Hamiltonian H to that of simulating a local Hamiltonian of the form $\tilde{H} = \sum_j c_j H_j$, where H_j 's are local operators [34]. While such mappings are

known to exist and form the cornerstone of Hamiltonian complexity theory [40], they have rarely been leveraged for algorithmic purposes. Hamiltonian embedding addresses this by providing explicit (i.e., “white-box”) constructions of the *embedding Hamiltonian* \tilde{H} through the introduction of ancilla qubits. Under an appropriate (hardware-aware) choice of embedding scheme, the locality of \tilde{H} may be much lower than that of H . In this regard, Hamiltonian embedding may be viewed as a time-space tradeoff that reduces locality at the cost of using a larger Hilbert space. In the following, we describe perturbative Hamiltonian embedding and explicit constructions for certain sparse matrices.

Let H be an n -dimensional Hermitian operator, denoted as the problem Hamiltonian. Assume there exists a q -qubit operator Q and subspace \mathcal{S} such that $Q|_{\mathcal{S}} = H$. Consider another q -qubit operator H^{pen} whose ground-energy subspace is precisely \mathcal{S} . H^{pen} is called the *penalty Hamiltonian* and \mathcal{S} is called the *embedding subspace*. Then, one can construct an embedding Hamiltonian

$$\tilde{H} = gH^{\text{pen}} + Q. \quad (3)$$

Relative to \mathcal{S} and \mathcal{S}^\perp , the off-diagonal blocks are denoted by $R := P_{\mathcal{S}^\perp} \tilde{H} P_{\mathcal{S}}$ (where $P_{\mathcal{S}}$ and $P_{\mathcal{S}^\perp}$ are projectors). When $\|R\|$ is sufficiently small relative to g , the dynamics of H are approximated by that of \tilde{H} , restricted to \mathcal{S} . Specifically, Ref. [34, Theorems 1 and 3] shows that the simulation error is bounded as

$$\left\| \left(e^{-i\tilde{H}t} \right) \Big|_{\mathcal{S}} - e^{-iHt} \right\| \leq (2\eta\|\tilde{H}\| + \epsilon)t, \quad (4)$$

where t is the evolution time, $\eta \sim \|R\|/g$ and $\epsilon \sim \|R\|/g$.

For applications, we not only require an embedding of H , but also embeddings of an observable O and input state $|\psi\rangle$, all using the same embedding subspace \mathcal{S} . Thus, Hamiltonian embedding may be viewed as a mapping of the triple $(H, O, |\psi\rangle)$ to $(\tilde{H}, \tilde{O}, |\tilde{\psi}\rangle)$. We note that for an n -qubit Hamiltonian H , taking $\mathcal{S} = \mathbb{C}^{2^n}$ corresponds to the trivial embedding $(H, O, |\psi\rangle) \mapsto (\tilde{H}, \tilde{O}, |\psi\rangle)$. Since each n -bit bitstring can be viewed as a binary representation of an integer $j \in \{0, \dots, 2^{n-1}\}$, this embedding is known as the *standard binary encoding*.

Explicit constructions of perturbative Hamiltonian embeddings were developed for embedding several sparse matrix structures. In particular, these embeddings are well-suited for banded and banded circulant matrices, but may also be applied to general sparse matrices. These embedding schemes are related to alternative encoding systems such as the unary and one-hot encodings, in contrast to the standard binary encoding.

The naive application of Hamiltonian embedding to a general unstructured $n \times n$ matrix may require $\mathcal{O}(n)$ qubits and $\mathcal{O}(n^2)$ terms, nullifying the potential of exponential quantum speedup. However, Ref. [34] shows that the Hamiltonian embedding technique preserves tensor product structure of the problem Hamiltonian. In other words, when H has appropriate tensor product structures, \tilde{H} can be constructed using resources that scale

as $\text{polylog}(n)$. This feature of Hamiltonian embedding allows the possibility of exponential quantum speedup, depending on the underlying application.

C. Relevant work

While early quantum PDE solvers relied on quantum linear system solvers [11, 41], variational quantum algorithms have gained prominence due to their lower resource requirements. Ref. [17] uses multiple copies of variational quantum states to solve nonlinear PDEs, and a similar approach was applied to solve Burgers' equation [42]. Ref. [43] develops a tensor-network based approach for simulating 1D linear Euler equations. Thus far, these variational approaches have been limited to problems in low dimensions and lack evidence for provable quantum speedup.

Recent quantum algorithms for simulating PDEs with theoretical guarantees primarily leverage algorithms for Hamiltonian simulation. Ref. [12] presents an algorithm for solving the advection equation by embedding the non-unitary time-evolution operator within a Hamiltonian simulation at each time step. Sato et al. [13] showed an efficient decomposition of finite difference operators via the Bell basis, which were used to simulate simple advection and wave equations exhibiting unitary dynamics. Subsequently, this approach was applied in conjunction with Schrödingerization to simulate non-unitary dynamics [44]. While this strategy could only be applied to PDEs with constant coefficients, Ref. [14] developed an algorithm for simulating PDEs with spatially varying coefficients via logic minimization. Despite these advances, the execution of these algorithms requires large fault-tolerant quantum computers and experimental demonstrations remain limited (a simulation of the 1D wave equation on 3 qubits was presented in Ref. [13]).

III. QUANTUM PDE SOLVERS VIA HAMILTONIAN EMBEDDING

Our general framework for simulating transport dynamics is based on the following problem:

Problem 1 (Simulation of k -th order linear PDEs). Let $d \geq 1$, $x \in \mathbb{R}^d$, and consider the linear PDE

$$\begin{aligned} \frac{\partial y}{\partial t} &= F(x, y, D_x y, \dots, D_x^k y), \\ y(0, x) &= y_0(x) \end{aligned} \quad (5)$$

where $y: \mathbb{R}^+ \times \mathbb{R}^d \rightarrow \mathbb{R}$ and $F: \mathbb{R}^d \times \mathbb{R} \times \mathbb{R}^d \times \dots \times \mathbb{R}^{d^k} \rightarrow \mathbb{R}$ is linear. Given an observable $f(x): \mathbb{R}^d \rightarrow \mathbb{R}$, evolution time $T > 0$, and precision $\epsilon > 0$, we consider the task of computing an ϵ -close approximation to $\int_{x \in \mathbb{R}^d} dx y(T, x)^\dagger f(x) y(T, x)$.

Problem 1 describes the simulation of general k -th order linear PDEs, which includes examples such as advection-diffusion equations, the Black-Scholes equation, or Maxwell's equation. Through linear representations of nonlinear PDEs, it also extends to some nonlinear PDEs such as scalar hyperbolic PDEs or Hamilton-Jacobi [45]. It does not contain other nonlinear PDEs such as the viscous Burgers' equation or the nonlinear reaction-diffusion equation (which instead may be solved via Carleman linearization [11, 46]).

In this paper, we focus on transport dynamics in d spatial dimensions, which could be linear or non-linear depending on the application. In case of nonlinearities, we first apply a linearization procedure to map the nonlinear PDE to a linear PDE in the form (5); the linearization procedure is standard [11, 47–49], and we omit it here for brevity.

Given a linear PDE, we discretize in space to obtain a linear ODE system of dimension N^d , where N is the number of grid points along each (spatial) dimension. Then, the discretized PDE is mapped to a unitary process (described by a sparse Hamiltonian) via Schrödingerization [27], followed by the Hamiltonian embedding [34] to obtain resource-efficient implementation on near- and intermediate-term devices. The overall algorithm is presented in Algorithm 1.

Algorithm 1: Quantum PDE solvers via Hamiltonian embedding

Input: Coefficient matrix $A = H_1 + iH_2$, observable O , evolution time T , precision ϵ

Output: Estimate of $u(t)^\dagger O u(t)$, where $u(t)$ is the solution to (7).

- 1 For $k = 1, \dots, d$, choose an embedding for the terms $h_{j,k}^{(1)}$ and $h_{j,k}^{(2)}$ comprising H_1 and H_2 in (10).
- 2 Use Hamiltonian embedding to map $(H, O, u(0))$ to $(\tilde{H}, \tilde{O}, \tilde{u}(0))$.
- 3 Apply Schrödingerization to simulate the embedded ODE:

$$\frac{d\tilde{u}(t)}{dt} = \tilde{H}\tilde{u}(t), \quad \tilde{u}(0) = \tilde{u}_0, \quad (6)$$

using a q -th order staged product formula for Hamiltonian simulation and Richardson extrapolation with error tolerance ϵ .

- 4 Return the ϵ -accurate estimate of $\tilde{u}(T)^\dagger \tilde{O}\tilde{u}(T)$.

A. Spatial discretization and Schrödingerization

In this work, we consider Eulerian discretizations using either finite differencing schemes or the Fourier spectral method.

When N grid points are used along each dimension, the discretization error along each dimension is typically

$\epsilon = \mathcal{O}(1/N)$ using finite differences (for instance, using the upwind scheme). For a PDE with d spatial variables, this results in $N = \mathcal{O}(d/\epsilon)$ to achieve an overall error ϵ . When periodic boundary conditions are imposed along a certain dimension, we may instead apply the Fourier spectral method. The advantage of spectral methods over finite difference schemes is that they result in spectral convergence, i.e. the error decreases faster than $\mathcal{O}(1/N^k)$ for all integers k [50]. We note that most suitable discretization scheme depends on the structure of the problem and that there is no single approach that works best in general.

Upon spatial discretization of (5) with N grid points along each dimension, we obtain the N^d -dimensional linear ODE:

$$\frac{du(t)}{dt} = Au(t), \quad u(0) = u_0, \quad (7)$$

where $A \in \mathbb{C}^{N^d \times N^d}$ and $u \in \mathbb{C}^{N^d}$. If O is a discretization of $f(x)$, then we can solve Problem 1 by simulating (7) on quantum computers and estimate the quantity $u(T)^\dagger Ou(T)$.

As we will see in Section III B, the use of Eulerian discretization schemes on regular grids allows us to exploit the tensor-product structure of A , which is the key to achieving exponential quantum speedup via Hamiltonian embedding. While other discretization methods (such as finite volume or finite element) are commonly used in classical numerical simulations [38, 51], proposed quantum algorithms for finite volumes [52] or finite elements [53–55] require sophisticated input models such as QRAM or block encodings due to the lack of a regular grid or mesh structure.

Having mapped the PDE to a finite-dimensional linear ODE, we apply Schrödingerization to embed the dynamics within a Hamiltonian simulation problem. The overall quantum circuit for Schrödingerization is depicted in Fig. 2.

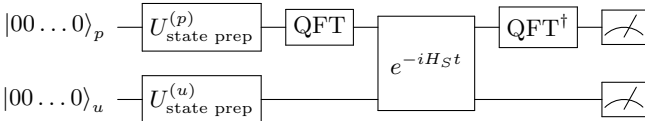


FIG. 2. Circuit diagram for Schrödingerization. The unitaries $U_{\text{state prep}}^{(p)}$ and $U_{\text{state prep}}^{(u)}$ denote state preparation circuits for the auxiliary variable p and the solution u , respectively.

In essence, the main computational cost is in simulating the Hamiltonian

$$H_S = H_1 \otimes H_{\mathcal{F}} - H_2 \otimes I, \quad (8)$$

where $H_1 + iH_2 = A$ and $H_{\mathcal{F}}$ is a diagonal matrix. Further details on the circuit implementation are provided in Appendix D 4.

B. Quantum simulation via Hamiltonian embedding

Next, we employ the Hamiltonian embedding technique to simulate the Schrödingerized linear ODE.

Definition 1 (Hamiltonian embeddings). Let $H \in \mathbb{C}^{N \times N}$ be a Hermitian operator, let $O \in \mathbb{C}^{N \times N}$ be a Hermitian observable, and $|\psi\rangle \in \mathbb{C}^N$ be a quantum state. Let \mathcal{S} be a subspace of \mathbb{C}^{2^q} for some integer $q \geq 1$ and let $P_{\mathcal{S}} : \mathbb{C}^N \rightarrow \mathcal{S}$ be an isometry. We say the triple $(\tilde{H}, \tilde{O}, |\tilde{\psi}\rangle)$ is a Hamiltonian embedding of $(H, O, |\psi\rangle)$ with embedding subspace \mathcal{S} if $P_{\mathcal{S}} \tilde{H} P_{\mathcal{S}}^\dagger = H$, $P_{\mathcal{S}} \tilde{O} P_{\mathcal{S}}^\dagger = O$, $P_{\mathcal{S}} |\tilde{\psi}\rangle = |\psi\rangle$, and \mathcal{S} is an invariant subspace of \tilde{H} .

Remark 1. Definition 1 is a special case of the more generally defined (i.e., perturbative) Hamiltonian embeddings in [34]. Our definition allows us to avoid introducing additional simulation error, leading to a more simplified presentation.

The Hamiltonian embedding technique provides a hardware-aware mapping of the *problem Hamiltonian* H to an *embedding Hamiltonian* \tilde{H} . When the mapping is chosen such that \tilde{H} is compatible with hardware-native operations, \tilde{H} admits a decomposition which leads to a resource-efficient implementation on hardware. Such a decomposition is essential for implementation on digital quantum computers. Alternatively, it may be the case that \tilde{H} can be directly simulated by the native device Hamiltonian of an analog quantum simulator; however, analog quantum simulators typically require geometrically local connectivity which poses a major difficulty for the simulation of high-dimensional PDEs. We leave a more detailed study of analog simulation of PDEs to future work (see [56] for a study using continuous variable quantum systems).

More concretely, we use and extend the one-hot, unary, and circulant unary embeddings developed in [34] to embed sparse matrices that commonly arise in the simulation of differential equations (see Appendix B for details). On the other hand, directly decomposing H (which may be viewed as a trivial embedding) is equivalent to using the standard binary encoding. Further discussions of the use of the standard binary encoding for representing certain diagonal and tridiagonal matrices are provided in Appendix C.

When discretizing a linear PDE via finite differences, the differential operators are mapped to sparse matrices which act nontrivially only along a single dimension. For instance, a first-order differential operator acting on a variable x_j is mapped as follows:

$$\frac{\partial y}{\partial x_j} \mapsto I \otimes \cdots \otimes \underbrace{A_j}_{j\text{-th term}} \otimes \cdots \otimes I, \quad (9)$$

where A_j is a spatially discretized differential operator acting on the register used to represent x_j . This local-

ity structure is essential for harnessing the exponential speedup offered by quantum computation. Leveraging this fact, we assume that A has Hermitian and anti-Hermitian parts H_1 and iH_2 that are succinctly represented by the following tensor product structure:

$$H_1 = \sum_{j=1}^{\Gamma} \gamma_j^{(1)} \bigotimes_{k=1}^d h_{j,k}^{(1)} \quad \text{and} \quad H_2 = \sum_{j=1}^{\Gamma} \gamma_j^{(2)} \bigotimes_{k=1}^d h_{j,k}^{(2)}, \quad (10)$$

where $\gamma_j^{(1)}, \gamma_j^{(2)} \in \mathbb{R}$ and $h_{j,k}^{(1)}$ and $h_{j,k}^{(2)}$ are sparse $N \times N$ matrices (e.g., diagonal, banded matrices, etc.).

Given the tensor product structure of H_1 and H_2 , we may apply Hamiltonian embedding to simulate linear ODEs. For $j = 1, 2, \dots, d$, we choose an embedding scheme for the j -th dimension. This enables us to embed each $h_{j,k}^{(1)}$ and $h_{j,k}^{(2)}$ as embedding Hamiltonians $\tilde{h}_{j,k}^{(1)}$ and $\tilde{h}_{j,k}^{(2)}$, where $\tilde{h}_{j,k}^{(1)}$ and $\tilde{h}_{j,k}^{(2)}$ can be further decomposed into a sum of multi-qubit operators. As a result, the non-Hermitian matrix H is mapped to $\tilde{H} = \tilde{H}_1 + i\tilde{H}_2$ where \tilde{H}_1 and \tilde{H}_2 are Hamiltonian embeddings of H_1 and H_2 , respectively.

To illustrate Hamiltonian embedding on a concrete example, consider a two-dimensional setting where for $m \in \{1, 2\}$, $H_m = I \otimes h_{1,2}^{(m)} + h_{2,1}^{(m)} \otimes I$ and all $h_{j,k}^{(m)}$ and $h_{j,k}^{(m)}$ are tridiagonal matrices. Then by embedding $h_{j,k}^{(m)}$ as $\tilde{h}_{j,k}^{(m)}$, we obtain the embedding Hamiltonians $\tilde{H}_m = I \otimes \tilde{h}_{1,2}^{(m)} + \tilde{h}_{2,1}^{(m)} \otimes I$. More generally, the embedding Hamiltonians admit decompositions

$$\tilde{H}_1 = \sum_{\ell=1}^L \alpha_{\ell}^{(1)} P_{\ell} \quad \text{and} \quad \tilde{H}_2 = \sum_{\ell=1}^L \alpha_{\ell}^{(2)} P_{\ell}, \quad (11)$$

where $\alpha_{\ell}^{(1)}, \alpha_{\ell}^{(2)} \in \mathbb{R}$ and P_{ℓ} 's are multi-qubit operators that may be efficiently exponentiated on quantum computers [57].

Given the decompositions (11), we construct the embedding Hamiltonian

$$\tilde{H}_S = \tilde{H}_1 \otimes H_F - \tilde{H}_2 \otimes I \quad (12)$$

and simulate the dynamics via product formulas.

C. Measurement and post-processing

In addition to embedding H_1 and H_2 , we embed the observable O as \tilde{O} and assume access to an embedded initial state $\tilde{u}(0)$, which when restricted to the embedding subspace, is proportional to $u(0)$. After applying Schrödingerization, we measure the p -register and post-select the outcomes in which $p > 0$. Then up to a constant factor, $u(t)^\dagger O u(t)$ is estimated by computing the expectation of \tilde{O} with respect to the system register.

While simulation with a p -th order product formula allows for gate complexity scaling nearly linearly in evolution time, the scaling in terms of precision is only

$\mathcal{O}(\epsilon^{-1/p})$. To match the optimal $\mathcal{O}(\log(1/\epsilon))$ dependence achieved by quantum signal processing [58], we incorporate classical extrapolation and post-processing.

Richardson extrapolation has emerged as an approach to improve the gate complexity of product formulas beyond $\mathcal{O}(1/\epsilon^p)$ for a p -th order product formula, while retaining desirable properties such as locality and commutator scaling [59]. Rather than estimating observable expectations using a fixed Trotter step size, the idea is to compute expectation values using a decreasing sequence of step sizes and extrapolate to the zero step size limit. Under this approach, it has been shown that in terms of evolution time T and precision ϵ , the maximum Trotter number scales as $\mathcal{O}(T^{(1+1/p)} \log(1/\epsilon))$. We leverage this approach to simulate the embedding Hamiltonian \tilde{H}_S with near-optimal gate complexity. Further details of product formulas and Richardson extrapolation for Hamiltonian simulation are provided in Appendix E 1.

D. Complexity Analysis

We analyze the runtime of Algorithm 1. The main computational cost comes from the use of Hamiltonian embedding as a subroutine. Using product formulas in conjunction with Richardson extrapolation, we achieve a gate complexity which scales nearly linearly in T and polylogarithmically in $1/\epsilon$.

Theorem 1 (PDE solvers using Hamiltonian embedding, informal). *Let H_1 and H_2 be Hamiltonians with Hamiltonian embeddings given by $\tilde{H}_1 = \sum_{\ell=1}^L \alpha_{\ell}^{(1)} P_{\ell}$ and $\tilde{H}_2 = \sum_{\ell=1}^L \alpha_{\ell}^{(2)} P_{\ell}$. Suppose \tilde{H}_1 and \tilde{H}_2 are both k -local, i.e. all P_{ℓ} act non-trivially on at most k qubits. Then to estimate $u(T)^\dagger O u(T)$ with relative error ϵ using a p -th order Υ -stage product formula, the total number of 1- and 2-qubit gates per circuit is*

$$\mathcal{O}\left(kL\Upsilon^{(2+1/p)}(\lambda T)^{(1+1/p)} \log(1/\epsilon)\right), \quad (13)$$

where λ is a nested commutator whose full expression is given in (E12).

We prove a more formal version of Theorem 1 in Appendix E 2. Our result achieves quasi-linear-in- T scaling, which is characteristic of high-order product formulas. While p -th order product formulas typically incur a gate complexity that scales as $\epsilon^{-1/p}$, the use of Richardson extrapolation allows us to improve the explicit dependence on ϵ to polylogarithmic in $1/\epsilon$. Additionally, we retain commutator scaling in the prefactor λ which we further bound in Appendix E 2. We note that in Theorem 1, the $\log(1/\epsilon)$ dependence only takes into account the error introduced by the quantum simulation algorithm. In the context of PDE simulation, discretization errors may require the norms of \tilde{H}_1 and \tilde{H}_2 to scale with $1/\epsilon$ (i.e., using finite difference schemes). As a result, the overall

gate complexity may depend polynomially in $1/\epsilon$. However, the end-to-end time complexity of any quantum algorithm for estimating observables is necessarily $\Omega(1/\epsilon)$, as dictated by the Heisenberg limit [60].

The choice of encoding scheme determines the structure (i.e., locality) of the embedding Hamiltonian and thereby affects the actual costs (i.e., gate counts and circuit depths) when implemented as quantum circuits. In particular, the one-hot and unary encodings allow $N \times N$ finite difference operators to be embedded using N -qubit Hamiltonians with nearest-neighbor interaction terms. In contrast, the standard binary encoding (for both the Pauli basis and Bell basis) decomposes finite difference operators using non-local operators on $\log_2(N)$ qubits (see Appendix C 2 for more details). In this sense, Hamiltonian embedding offers a time-space tradeoff in which spatial resources are used to map the problem Hamiltonian to an embedding Hamiltonian whose dynamics can be more easily simulated on hardware.

The particular pattern of Hamiltonian embedding often enables a *gate-level parallelization* that reduces the circuit depth through the use of additional ancilla qubits. Note that Schrödingerization involves controlled Hamiltonian simulation, a naive implementation requires each controlled gate to be applied consecutively. This overhead can be circumvented by encoding each ancilla qubit using a repetition code whose length is equal to the number of system (non-ancilla) qubits. This way, the circuit depth can be reduced by a factor proportional to the number of qubits used. In particular, Hamiltonian embeddings such as one-hot or unary allow for a circuit depth reduction by an $O(N)$ factor, while the standard binary encoding can only benefit by an $O(\log(N))$ factor.

IV. LINEAR TRANSPORT DYNAMICS

A. Problem formulation

Linear advection equations serve as prototypical examples of hyperbolic PDEs that model the transport of heat or fluids. Here, we consider a constant velocity advection equation in d spatial dimensions given by

$$\frac{\partial u}{\partial t} + c \cdot \nabla u = 0, \quad (14)$$

$$u(0, x) = u_0(x), \quad (15)$$

where $c = (c_1, \dots, c_d) \in \mathbb{R}^d$ and $x \in [0, 1]^d$ with periodic boundary conditions.

B. Construction of Hamiltonian embedding

To simulate the advection dynamics, we discretize in space using centered differences (see Appendix A) and

obtain the linear ODE (7) with coefficient matrix

$$A = -i \sum_{j=1}^d c_j (I \otimes \cdots \otimes \underbrace{A_j}_{j\text{th term}} \otimes \cdots \otimes I), \quad (16)$$

where A_j 's are circulant tridiagonal matrices with $-i$ on the superdiagonal and $+i$ on the subdiagonal. We use the one-hot embedding to embed each A_j , obtaining the embedding Hamiltonian

$$H_{\text{adv}} = -\frac{1}{2h} \sum_{j=1}^d \sum_{k=1}^N c_j \left(\frac{X_{k+1}^{(j)} Y_k^{(j)} - Y_{k+1}^{(j)} X_k^{(j)}}{2} \right), \quad (17)$$

where $N = 10$, $h = 1/N$, $d = 2$, and $c_j = 1$ for all $j = 1, \dots, d$. Since the use of centered differences results in unitary dynamics, Schrödingerization both straightforwardly reduce to Hamiltonian simulation without requiring additional ancilla qubits.

C. Demonstration using quantum computers

We validate our approach by a real-machine demonstration of an advection equation in $d = 2$ spatial dimensions on the IonQ Aria-1 quantum computer [61]. We choose the initial state to be two Gaussian peaks, and set the velocity vector to $(c_1, c_2) = (1, 1)$. We simulate H_{adv} for time up to $T = 0.2$ using the second-order Trotter-Suzuki formula. Due to the limitations of hardware noise, we do not perform Richardson extrapolation; instead, we apply the second-order Trotter-Suzuki formula and limit the number of Trotter steps to a maximum of two steps, resulting in a maximum gate count of 212 single-qubit gates and 115 two-qubit gates. The real-machine demonstration results are shown in Fig. 3. Notably, despite a significantly lower resolution than the classical simulation, the experimental results clearly capture the direction and drift velocity of the Gaussian waves.

D. Resource analysis

We conduct a resource analysis for simulating (14) using the upwind scheme. This setting represents the typical scenario in which the dynamics are non-unitary and is simulated using Schrödingerization.

We compare the standard binary encoding (with the Pauli basis or Bell basis decompositions), the penalty-free one-hot embedding, and the penalty-free circulant unary embedding. For all encoding schemes, we simulate the dynamics using the second-order Trotter-Suzuki formula. We numerically compute the Trotter error for a single step for time T/r , then use the triangle inequality to estimate the error for r Trotter steps. Binary search is used to estimate the Trotter number required to reach an error below $\epsilon = 5 \times 10^{-2}$. We use Qiskit [62] to optimize and compile the circuits to single qubit Pauli

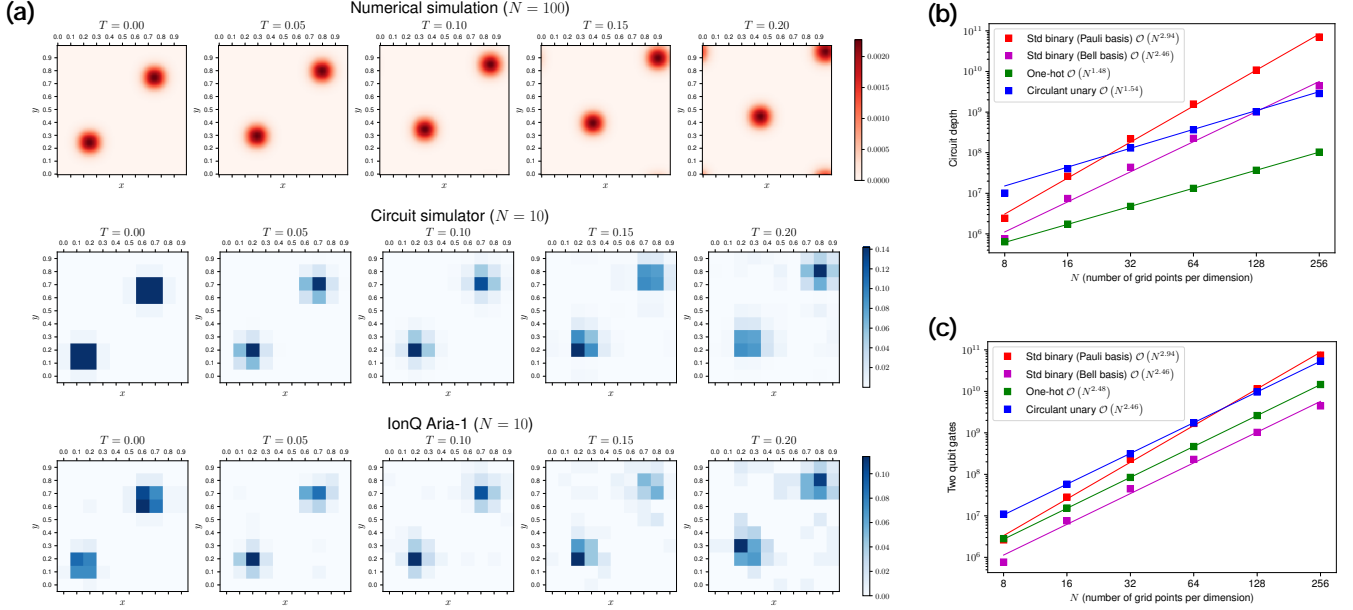


FIG. 3. **Quantum simulation of the 2D linear advection equation.** **Left:** (a) Each row shows the measured probability distribution for simulation times $T \in \{0, 0.05, 0.10, 0.15, 0.20\}$ (left to right). A high resolution classical simulation is shown in the top row for reference. The middle row shows results obtained from a noiseless circuit simulation, and the bottom row shows the results obtained from the Aria-1 quantum computer. **Right:** Empirical estimates of the two-qubit circuit depth (b) and gate count (c) required to simulate the advection equation with the upwind differences and Schrödingerization.

rotations and XX rotation gates, using all-to-all device connectivity. Furthermore, we employ the parallelization technique to optimize the circuit depth for the standard binary (Pauli basis), one-hot, and unary encodings.

Our estimates of the two-qubit circuit depth and gate counts are shown in Fig. 3 (b) and (c), respectively (see Appendix F for explicit counts). In terms of the circuit depth, the sparse encodings (one-hot and circulant unary) yield the most favorable asymptotic scaling (roughly $O(N^{3/2})$ from second-order Trotter). Overall, the one-hot encoding yields the shallowest circuits, followed by the Bell basis for $N \leq 64$. In particular, the one-hot encoding achieves a $42 \times$ reduction in circuit depth for $N = 256$. The Bell basis tends to use the fewest two-qubit gates; however, all methods are within roughly an order of magnitude of each other.

V. NONLINEAR TRANSPORT DYNAMICS

A. Problem formulation

Quantum computers are best suited for simulating linear dynamics due to the linearity of quantum mechanics. However, many physical phenomena involve nonlinearity which poses a challenge for classical and quantum simulation alike. Fortunately, certain classes of nonlinear PDEs can be mapped to linear dynamics and solved efficiently via quantum simulation.

Here, we consider a $(d+1)$ -dimensional nonlinear scalar

hyperbolic PDE given by

$$\begin{aligned} \partial_t u + G(u) \cdot \nabla u &= 0, \\ u(0, x) &= u_0(x), \end{aligned} \quad (18)$$

where $x \in \mathbb{R}^d$ and $u : \mathbb{R}^+ \times \mathbb{R}^d \rightarrow \mathbb{R}$. This PDE captures nonlinearity through the coefficient function $G(u)$ and is a generalization of the inviscid Burgers' equation commonly studied in fluid dynamics. To handle the nonlinearity, (18) can be represented as a linear PDE using the level set method [45]. Introducing an auxiliary variable q , we apply the level set method and solve for $\phi(t, x, q)$ satisfying

$$\begin{aligned} \frac{\partial \phi}{\partial t} + G(q) \cdot \nabla \phi &= 0, \\ \phi(0, x, q) &= \delta(q - u_0(x)), \end{aligned} \quad (19)$$

for which the solution is known to satisfy $\phi(t, x, q) = \delta(q - u(t, x))$ [49].

For concreteness, we consider the numerical simulation of (19) in two dimensions where $x = (x_1, x_2) \in [0, 1]^2$, $q \in [-1, 1]$, and $G(u) = u^3(1 - u^4)$. While finite differences may be used to discretize in space, the initial condition being a delta function results in poor numerical accuracy. To avoid this issue, we instead use the Fourier spectral method in which we apply the Fourier transform to x and simulate (19) in the frequency basis.

On a quantum computer, our simulation of (19) involves a quantum register for each of the variables x_1 , x_2 , and q . We first apply the quantum Fourier transform

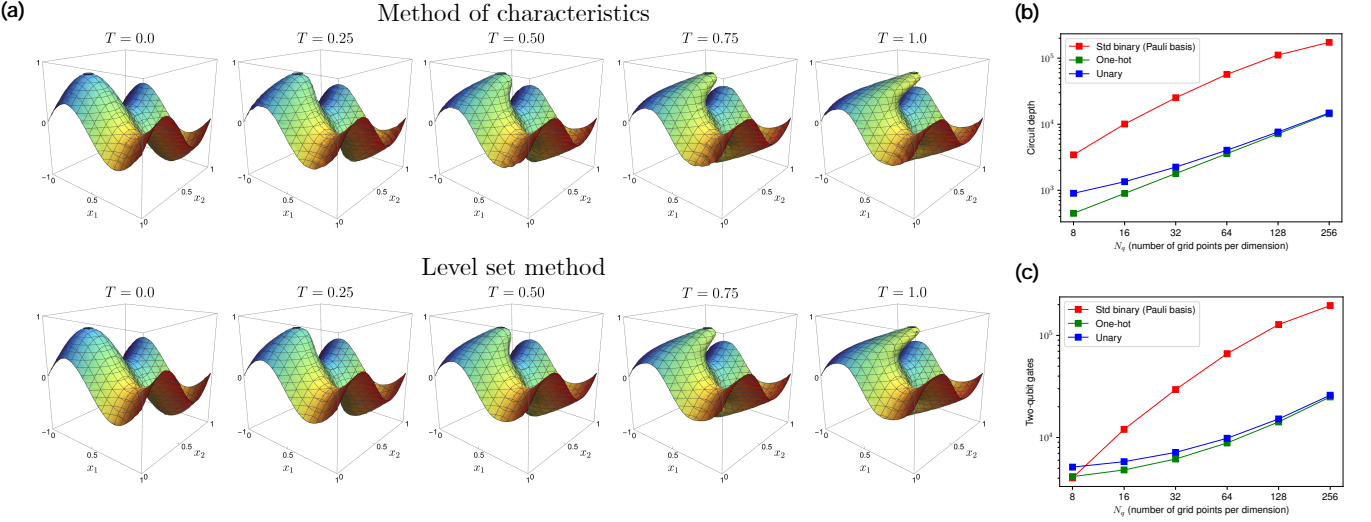


FIG. 4. **Quantum simulation of nonlinear transport dynamics.** **Left:** (a) Numerical simulations of (18) for times $T \in \{0, 0.25, 0.50, 0.75, 1.0\}$ using the method of characteristics (top) and the level set method (bottom). The initial condition is $u_0(x_1, x_2) = 0.4(\sin(2\pi x_1) + \sin(2\pi x_2))$. We discretize using $N_x = N_q = 128$ grid points for each dimension. **Right:** Empirical estimates of the two-qubit circuit depth (b) and gate counts (c) for simulating (18) using N_q grid points for q , where $N_q \in \{8, 16, 32, 64, 128\}$.

to the registers for x_1 and x_2 . In the frequency basis, we simulate the diagonal Hamiltonian H_d given by

$$H_d = D_{x_1} \otimes I \otimes D_q + I \otimes D_{x_2} \otimes D_q, \quad (20)$$

where $D_{x_1} = D_{x_2}$ is a diagonal matrix of Fourier frequencies and D_q is a diagonal matrix encoding values of $G(q)$. Finally, we recover the numerical solution by applying inverse QFT to each of x_1 and x_2 . We note that the QFT and simulation of H_d are all done in the appropriate embedding chosen for each of the variables x_1 , x_2 , and q .

B. Construction of Hamiltonian embedding

To embed the Hamiltonian H_d , we use the standard binary encoding of x_1 and x_2 , while allowing freedom to choose an embedding for q . The use of the standard binary encoding for x_1 and x_2 is justified by the fact that $D_{x_1} = D_{x_2} = \text{diag}(0, 1, \dots, N/2 - 1, -N/2, -N/2 + 1, \dots, -1)$ is a diagonal matrix of Fourier frequencies. As shown in Appendix C, this matrix has a 1-local Pauli decomposition given by

$$D_{x_1} = D_{x_2} = -\frac{1}{2} \left(I - 2^n Z_n + \sum_{j=1}^n 2^{j-1} Z_j \right). \quad (21)$$

Compared to sparse embedding such as one-hot or unary embeddings, the standard binary encoding is particularly suitable for representing x_1 and x_2 since it only requires $O(\log N)$ qubits while retaining a low locality Pauli decomposition.

Since $G(u)$ is a degree-4 polynomial, the best choice of embedding q is not immediately clear. Thus, we consider various embeddings of D_q and analyze the resulting circuit depths. As an example, applying the one-hot embedding to embed D_q results in the embedding Hamiltonian

$$\tilde{D}_q = \sum_{j=1}^N G(q_j) \hat{n}_j^{(1)}, \quad (22)$$

where $\hat{n}_j^{(1)} = \frac{1}{2} (I - Z_j)$ and q_j is the j -th grid point on the discretized interval $[-1, 1]$.

The resulting overall embedding Hamiltonian is given by

$$\tilde{H}_d = \tilde{D}_{x_1} \otimes I \otimes \tilde{D}_q + I \otimes \tilde{D}_{x_2} \otimes \tilde{D}_q, \quad (23)$$

where $D_{x_j} = \tilde{D}_{x_j}$ due to the use of the standard binary encoding of x_1 and x_2 .

C. Numerical simulation

Our numerical simulation of the level set method via the Fourier spectral method is shown in the bottom row of Fig. 4. We verify correctness by comparing against the method of characteristics, which are shown in the top row. We emphasize that while the results of Fig. 4 are classically simulated, they are mathematically equivalent to a circuit-level simulation on quantum computers.

D. Resource analysis

We perform a resource analysis to compare the circuit depths required to simulate (19) when using different embedding schemes. We compare the standard binary, one-hot, and unary embeddings for q , while the standard binary code is used to encode x_1 and x_2 . Additionally, we parallelize the gates by introducing an ancilla qubit for each qubit used to represent q . This is enabled by the fact that the simulation of H_d can be viewed as Hamiltonian simulation of D_q controlled on each qubit used to represent x_1 and x_2 .

The estimated circuit depths and two-qubit gate counts are presented in Fig. 4 (b) and (c), respectively. In general, the one-hot and unary embeddings outperform the standard binary code. We emphasize that this is a direct consequence of the choice of embedding \tilde{D}_q for the matrix D_q . For the unary and one-hot embeddings, \tilde{D} consists of identity and single-site Pauli- Z operators. On the other hand, the naive Pauli decomposition of D_q generally contains 4-local terms since $G(u)$ is a degree-4 polynomial. As a result, simulating \tilde{D}_q using the unary and one-hot embeddings is significantly cheaper than a direct simulation of D_q , in terms of both circuit depth and gate counts. This underscores the importance of choosing the right embedding for each problem, which can drastically influence the overall simulation cost.

VI. DISCUSSION AND CONCLUSIONS

In this paper, we developed a framework for resource-efficient simulation of transport dynamics. Our use of Hamiltonian embedding enables the end-to-end implementation of differential equation solvers without sophisticated quantum circuit constructions. Through extensive resource analyses, we find that certain embedding schemes are better suited for solving PDEs with certain mathematical structure. In particular, sparse encodings such as the one-hot or unary codes are best suited for embedding finite difference operators and benefit most from parallelization of controlled Hamiltonian simulation. Our approach fully addresses the difficulty of loading sparse Hamiltonians that arise from quantum simulation of transport dynamics with wide applicability to various PDE structures (e.g., spatially varying coefficients). Furthermore, our use of product formulas and Richardson extrapolation make our algorithm suitable for intermediate-term and early fault-tolerant devices while retaining near-optimal asymptotic gate complexity.

While linear dynamics are most amenable to be solved via quantum simulation, our framework also encapsulates broader families of PDEs through the process of linearization. In this work, we explored the use of the level set method, which are limited to nonlinear scalar hyperbolic PDEs and Hamilton-Jacobi equations [45]. It remains an open question whether other families of nonlinear PDEs

offer linear representations that can then be solved via Hamiltonian simulation.

For practically useful applications of quantum differential equation solvers, there remain several limitations that remain unaddressed in our work. For example, practical applications often require an initial state that is non-trivial to prepare. While there are several proposed algorithms for preparing certain quantum states [63–65], these methods either require coherent arithmetic or are formulated using sophisticated input models, making them impractical for intermediate-term quantum computers. Developing more efficient initial state preparation schemes that are feasible for near-term quantum hardware remains relatively unexplored. Furthermore, our real-machine demonstrations are limited in scale due to the rapid decoherence of NISQ-era devices. As the capabilities of quantum hardware advance, we anticipate greater applicability of quantum differential equation solvers to real-world problems.

ACKNOWLEDGMENT

We thank Dong An for helpful discussions. This work was partially funded by the U.S. Department of Energy, Office of Science, Office of Advanced Scientific Computing Research, Accelerated Research in Quantum Computing under Award Number DESC0020273 and DESC0025341, the Air Force Office of Scientific Research under Grant No. FA95502110051, the U.S. National Science Foundation grant CCF-1816695 and CCF-1942837 (CAREER), and a Sloan research fellowship. Jiaqi Leng is partially supported by DOE QSA Grant No. FP00010905, a Simons Quantum Postdoctoral Fellowship, and a Simons Investigator award through Grant No. 825053. We are also grateful to the access to IonQ machines provided by the National Quantum Laboratory (QLab) at UMD.

[1] J. D. Anderson and J. Wendt, *Computational fluid dynamics*, Vol. 206 (Springer, 1995).

[2] D. J. Tritton, *Physical fluid dynamics* (Springer Science & Business Media, 2012).

[3] R. B. Rood, Numerical advection algorithms and their role in atmospheric transport and chemistry models, *Reviews of Geophysics* **25**, 71 (1987).

[4] H. Fogler, *Elements of Chemical Reaction Engineering*, International Series in the Physical and Chemical Engineering Sciences (Pearson Education, 2020).

[5] O. G. Jepps and L. Rondoni, Thermodynamics and complexity of simple transport phenomena, *Journal of Physics A: Mathematical and General* **39**, 1311 (2006).

[6] E. P. Alves and F. Fiuza, Data-driven discovery of reduced plasma physics models from fully kinetic simulations, *Phys. Rev. Res.* **4**, 033192 (2022).

[7] J. S. Hesthaven, G. Rozza, B. Stamm, *et al.*, *Certified reduced basis methods for parametrized partial differential equations*, Vol. 590 (Springer, 2016).

[8] R. J. Kee, M. E. Coltrin, P. Glarborg, and H. Zhu, *Chemically reacting flow: Theory, modeling, and simulation* (John Wiley & Sons, 2017).

[9] R. P. Feynman, Simulating physics with computers, *International Journal of Theoretical Physics* **21**, 467 (1982).

[10] A. M. Childs, R. Kothari, and R. D. Somma, Quantum algorithm for systems of linear equations with exponentially improved dependence on precision, *SIAM Journal on Computing* **46**, 1920 (2017).

[11] J.-P. Liu, H. Øie Kolden, H. K. Krovi, N. F. Loureiro, K. Trivisa, and A. M. Childs, Efficient quantum algorithm for dissipative nonlinear differential equations, *Proceedings of the National Academy of Sciences* **118**, e2026805118 (2021), <https://www.pnas.org/doi/pdf/10.1073/pnas.2026805118>.

[12] P. Brearley and S. Laizet, Quantum algorithm for solving the advection equation using Hamiltonian simulation, *Phys. Rev. A* **110**, 012430 (2024).

[13] Y. Sato, R. Kondo, I. Hamamura, T. Onodera, and N. Yamamoto, Hamiltonian simulation for hyperbolic partial differential equations by scalable quantum circuits, *Physical Review Research* **6**, 033246 (2024).

[14] Y. Sato, H. Tezuka, R. Kondo, and N. Yamamoto, Quantum algorithm for partial differential equations of non-conservative systems with spatially varying parameters (2024), arXiv:2407.05019 [quant-ph].

[15] A. A. Zecchi, C. Sanavio, S. Perotto, and S. Succi, Improved amplitude amplification strategies for the quantum simulation of classical transport problems, *Quantum Science and Technology* **10**, 035039 (2025).

[16] X. Li, X. Yin, N. Wiebe, J. Chun, G. K. Schenter, M. S. Cheung, and J. Mülmenstädt, Potential quantum advantage for simulation of fluid dynamics, *Phys. Rev. Res.* **7**, 013036 (2025).

[17] M. Lubasch, J. Joo, P. Moinier, M. Kiffner, and D. Jaksch, Variational quantum algorithms for nonlinear problems, *Phys. Rev. A* **101**, 010301 (2020).

[18] O. Kyriienko, A. E. Paine, and V. E. Elfving, Solving nonlinear differential equations with differentiable quantum circuits, *Phys. Rev. A* **103**, 052416 (2021).

[19] R. Demirdjian, D. Gunlycke, C. A. Reynolds, J. D. Doyle, and S. Tafur, Variational quantum solutions to the advection-diffusion equation for applications in fluid dynamics, *Quantum Information Processing* **21**, 322 (2022).

[20] P. Over, S. Bengoechea, T. Rung, F. Clerici, L. Scandurra, E. de Villiers, and D. Jaksch, Boundary treatment for variational quantum simulations of partial differential equations on quantum computers (2024), arXiv:2402.18619 [quant-ph].

[21] M. Umer, E. Mastorakis, S. Evangelou, and D. G. Angelakis, Nonlinear quantum dynamics in superconducting NISQ processors (2024), arXiv:2403.16426 [quant-ph].

[22] H. Jaffali, J. B. de Araujo, N. Milazzo, M. Reina, H. de Boutray, K. Baumann, F. Holweck, Y. Mohdeb, and R. Katz, H-DES: a quantum-classical hybrid differential equation solver, arXiv preprint arXiv:2410.01130 10.48550/arXiv.2410.01130 (2024).

[23] D. W. Berry, High-order quantum algorithm for solving linear differential equations, *Journal of Physics A: Mathematical and Theoretical* **47**, 105301 (2014).

[24] H. Krovi, Improved quantum algorithms for linear and nonlinear differential equations, *Quantum* **7**, 913 (2023).

[25] D. W. Berry and P. C. Costa, Quantum algorithm for time-dependent differential equations using Dyson series, *Quantum* **8**, 1369 (2024).

[26] P. C. S. Costa, S. Jordan, and A. Ostrander, Quantum algorithm for simulating the wave equation, *Phys. Rev. A* **99**, 012323 (2019).

[27] S. Jin, N. Liu, and Y. Yu, Quantum simulation of partial differential equations: Applications and detailed analysis, *Phys. Rev. A* **108**, 032603 (2023).

[28] D. An, J.-P. Liu, and L. Lin, Linear combination of Hamiltonian simulation for nonunitary dynamics with optimal state preparation cost, *Phys. Rev. Lett.* **131**, 150603 (2023).

[29] R. Babbush, D. W. Berry, R. Kothari, R. D. Somma, and N. Wiebe, Exponential quantum speedup in simulating coupled classical oscillators, *Phys. Rev. X* **13**, 041041 (2023).

[30] L. Wright, C. M. Keever, J. T. First, R. Johnston, J. Tillay, S. Chaney, M. Rosenkranz, and M. Lubasch, Noisy intermediate-scale quantum simulation of the one-dimensional wave equation (2024), arXiv:2402.19247 [quant-ph].

[31] D. Aharonov and A. Ta-Shma, Adiabatic quantum state generation and statistical zero knowledge, in *Proceedings of the Thirty-Fifth Annual ACM Symposium on Theory of Computing*, STOC '03 (Association for Computing Machinery, New York, NY, USA, 2003) p. 20–29.

[32] A. Gilyén, Y. Su, G. H. Low, and N. Wiebe, Quantum singular value transformation and beyond: exponential improvements for quantum matrix arithmetics, in *Proceedings of the 51st Annual ACM SIGACT Symposium on Theory of Computing*, STOC 2019 (Association for Computing Machinery, New York, NY, USA, 2019) p. 193–204.

[33] V. Giovannetti, S. Lloyd, and L. Maccone, Quantum random access memory, *Phys. Rev. Lett.* **100**, 160501 (2008).

[34] J. Leng, J. Li, Y. Peng, and X. Wu, Expanding hardware-efficiently manipulable Hilbert space via Hamiltonian embedding (2024), arXiv:2401.08550 [quant-ph].

[35] T. Xin, S. Wei, J. Cui, J. Xiao, I. n. Arrazola, L. Lamata, X. Kong, D. Lu, E. Solano, and G. Long, Quantum algorithm for solving linear differential equations: Theory and experiment, *Phys. Rev. A* **101**, 032307 (2020).

[36] S. Jin and N. Liu, Quantum simulation of discrete linear dynamical systems and simple iterative methods in linear algebra via Schrödingerisation (2023), arXiv:2304.02865 [quant-ph].

[37] D. P. Chock and A. M. Dunker, A comparison of numerical methods for solving the advection equation, *Atmospheric Environment* (1967) **17**, 11 (1983).

[38] R. J. LeVeque, *Finite volume methods for hyperbolic problems*, Vol. 31 (Cambridge university press, 2002).

[39] D. W. Berry, A. M. Childs, and R. Kothari, Hamiltonian simulation with nearly optimal dependence on all parameters, in *2015 IEEE 56th annual symposium on foundations of computer science* (IEEE, 2015) pp. 792–809.

[40] T. S. Cubitt, A. Montanaro, and S. Piddock, Universal quantum hamiltonians, *Proceedings of the National Academy of Sciences* **115**, 9497 (2018).

[41] A. M. Childs and J.-P. Liu, Quantum spectral methods for differential equations, *Communications in Mathematical Physics* **375**, 1427 (2020).

[42] D. Jaksch, P. Givi, A. J. Daley, and T. Rung, Variational quantum algorithms for computational fluid dynamics, *AIAA journal* **61**, 1885 (2023).

[43] P. Siegl, G. S. Reese, T. Hashizume, N.-L. van Hülst, and D. Jaksch, Tensor-programmable quantum circuits for solving differential equations, *Phys. Rev. Res.* **8**, 013052 (2026).

[44] J. Hu, S. Jin, N. Liu, and L. Zhang, Quantum circuits for partial differential equations via Schrödingerisation (2024), arXiv:2403.10032 [quant-ph].

[45] S. Jin and S. Osher, A level set method for the computation of multi-valued solutions to quasi-linear hyperbolic PDEs and Hamilton-Jacobi equations, *Communications in Mathematical Sciences* **1**, 575 (2003).

[46] J.-P. Liu, D. An, D. Fang, J. Wang, G. H. Low, and S. Jordan, Efficient quantum algorithm for nonlinear reaction–diffusion equations and energy estimation, *Communications in Mathematical Physics* **404**, 963 (2023).

[47] S. K. Leyton and T. J. Osborne, A quantum algorithm to solve nonlinear differential equations (2008), arXiv:0812.4423 [quant-ph].

[48] I. Joseph, Koopman–von Neumann approach to quantum simulation of nonlinear classical dynamics, *Phys. Rev. Res.* **2**, 043102 (2020).

[49] S. Jin and N. Liu, Quantum algorithms for computing observables of nonlinear partial differential equations (2022), arXiv:2202.07834 [quant-ph].

[50] J. Boyd, *Chebyshev and Fourier Spectral Methods: Second Revised Edition*, Dover Books on Mathematics (Dover Publications, 2001).

[51] S. C. Brenner and L. R. Scott, *The mathematical theory of finite element methods* (Springer, 2008).

[52] Z.-Y. Chen, C. Xue, S.-M. Chen, B.-H. Lu, Y.-C. Wu, J.-C. Ding, S.-H. Huang, and G.-P. Guo, Quantum finite volume method for computational fluid dynamics with classical input and output, arXiv preprint arXiv:2102.03557 10.48550/arXiv.2102.03557 (2021).

[53] B. D. Clader, B. C. Jacobs, and C. R. Sprouse, Preconditioned quantum linear system algorithm, *Phys. Rev. Lett.* **110**, 250504 (2013).

[54] A. Montanaro and S. Pallister, Quantum algorithms and the finite element method, *Phys. Rev. A* **93**, 032324 (2016).

[55] M. Deiml and D. Peterseim, Quantum realization of the finite element method, *Mathematics of Computation* 10.1090/mcom/4137 (2025).

[56] S. Jin and N. Liu, Analog quantum simulation of partial differential equations, *Quantum Science and Technology* **9**, 035047 (2024).

[57] While the Hamiltonian embeddings proposed in [34] yield $P_\ell^{(1)}$ and $P_\ell^{(2)}$ as multi-qubit Pauli operators, we note that other decompositions are possible. For instance, the Bell basis decomposition of finite difference operators [13] may be viewed as a special case of Hamiltonian embedding. We assume that if P_ℓ is a k -qubit operator, then it may be exponentiated with $\mathcal{O}(k)$ 1- and 2-qubit gates, which is the case for both multi-qubit Pauli operators and Bell basis operators.

[58] G. H. Low and I. L. Chuang, Optimal Hamiltonian simulation by quantum signal processing, *Phys. Rev. Lett.* **118**, 010501 (2017).

[59] J. D. Watson and J. Watkins, Exponentially reduced circuit depths using trotter error mitigation, *PRX Quantum* **6**, 030325 (2025).

[60] M. Zwierz, C. A. Pérez-Delgado, and P. Kok, General optimality of the Heisenberg limit for quantum metrology, *Phys. Rev. Lett.* **105**, 180402 (2010).

[61] The Aria-1 quantum computer is a trapped-ion device with all-to-all connectivity. At the time the circuits were executed, the SPAM error was 0.62%, the 1-qubit gate fidelity was 0.9998, and the 2-qubit gate fidelity was 0.9871 as reported by IonQ’s device characterization.

[62] Qiskit contributors, Qiskit: An open-source framework for quantum computing (2023).

- [63] L. Grover and T. Rudolph, Creating superpositions that correspond to efficiently integrable probability distributions (2002), arXiv:quant-ph/0208112 [quant-ph].
- [64] A. G. Rattew and B. Koczor, Preparing arbitrary continuous functions in quantum registers with logarithmic complexity (2022), arXiv:2205.00519 [quant-ph].
- [65] S. McArdle, A. Gilyén, and M. Berta, Quantum state preparation without coherent arithmetic (2022), arXiv:2210.14892 [quant-ph].
- [66] R. J. LeVeque, *Finite difference methods for ordinary and partial differential equations: steady-state and time-dependent problems* (SIAM, 2007).
- [67] E. Bäumer and S. Woerner, Measurement-based long-range entangling gates in constant depth, *Phys. Rev. Res.* **7**, 023120 (2025).
- [68] B. Arseniev, D. Guskov, R. Sengupta, J. Biamonte, and I. Zacharov, Tridiagonal matrix decomposition for Hamiltonian simulation on a quantum computer, *Phys. Rev. A* **109**, 052629 (2024).
- [69] B. L. Douglas and J. B. Wang, Efficient quantum circuit implementation of quantum walks, *Phys. Rev. A* **79**, 052335 (2009).
- [70] D. An, A. M. Childs, and L. Lin, Quantum algorithm for linear non-unitary dynamics with near-optimal dependence on all parameters (2023), arXiv:2312.03916 [quant-ph].
- [71] Y. Tong, D. An, N. Wiebe, and L. Lin, Fast inversion, preconditioned quantum linear system solvers, fast green's-function computation, and fast evaluation of matrix functions, *Phys. Rev. A* **104**, 032422 (2021).
- [72] A. M. Childs, Y. Su, M. C. Tran, N. Wiebe, and S. Zhu, Theory of Trotter error with commutator scaling, *Phys. Rev. X* **11**, 011020 (2021).
- [73] S. Chakraborty, S. Hazra, T. Li, C. Shao, X. Wang, and Y. Zhang, Quantum singular value transformation without block encodings: Near-optimal complexity with minimal ancilla, arXiv preprint arXiv:2504.02385 10.48550/arXiv.2504.02385 (2025).
- [74] S. Jin, N. Liu, and C. Ma, On Schrödingerization-based quantum algorithms for linear dynamical systems with inhomogeneous terms (2025).

APPENDICES

Acknowledgment	10
A. Finite difference schemes for hyperbolic PDEs	14
1. Centered differences	14
2. Upwind scheme	15
B. Hamiltonian embeddings of sparse matrices	15
1. Penalty-free embedding schemes	16
One-hot embedding	16
Unary embedding	16
Circulant unary embedding	17
C. Standard binary encodings of sparse matrices	17
1. Polynomial functions	17
2. Finite difference operators	19
D. Quantum simulation of non-unitary dynamics	19
1. Linear combination of Hamiltonian simulation	19
2. Schrödingerization	20
3. Proof of Schrödingerization	21
4. Implementation of Schrödingerization	22
E. Quantum ODE solvers using Hamiltonian embedding	23
1. Hamiltonian simulation via product formulas and Richardson extrapolation	23
2. Complexity analysis for Algorithm 1	25
F. Resource estimates for the advection equation and nonlinear scalar hyperbolic PDE.	26
G. Comparison between Schrödingerization and LCHS	27

Appendix A: Finite difference schemes for hyperbolic PDEs

In this section, we review spatial discretization schemes for hyperbolic partial differential equations.

For illustrative purposes, we consider the discretization for the 1-dimensional variable coefficient case, in which

$$\frac{\partial u}{\partial t} = -f(x) \frac{\partial u}{\partial x}. \quad (\text{A1})$$

Here we have not yet specified the boundary conditions. The stability of the discretization scheme depends on the boundary conditions, and the chosen scheme ultimately determines the Hamiltonian to be simulated. For all discretization schemes, the method of lines yields an ODE system

$$\frac{d\mathbf{u}(t)}{dt} = A\mathbf{u}(t), \quad (\text{A2})$$

and $\mathbf{u}(t) = [u_1(t), u_2(t), \dots, u_N(t)]^\top$ denotes the vectorized mesh function and A is a coefficient matrix which depends on the scheme chosen.

1. Centered differences

The centered differences scheme is stable only for periodic boundary conditions. We discretize (A1) using N grid points and let $h = 1/N$ be the distance between grid points. Let $u_j(t)$ denote the value of $u(t, x)$ at the j -th grid point upon applying discretization. Let q_1, \dots, q_N be equally spaced grid points such that $q_1 < \dots < q_N$, identifying q_{N+1}

with q_1 . For symmetry, let $q_{j+1/2} = (q_j + q_{j+1})/2$ be the midpoint for the j -th subinterval. By centered differences, we obtain the discretization scheme

$$\frac{du_j}{dt} = - \left(\frac{f(q_{j+1/2})u_{j+1} - f(q_{j-1/2})u_{j-1}}{2h} \right) + \frac{f'(q_j)}{2}u_j + \mathcal{O}(h), \quad (\text{A3})$$

for all j . If $f(x)$ has the same periodic boundary condition as $u(x)$ does, thus (A3) can be written as the ODE system (A2) with coefficient matrix

$$A_c = \begin{pmatrix} \frac{f'(q_1)}{2} & -\frac{f(q_{1+1/2})}{2h} & & \frac{f(q_{N+1/2})}{2h} \\ \frac{f(q_{1+1/2})}{2h} & \frac{f'(q_2)}{2} & \ddots & \\ & \ddots & \ddots & \ddots \\ & & \ddots & -\frac{f(q_{N-1/2})}{2h} \\ -\frac{f(q_{N+1/2})}{2h} & & \frac{f(q_{N-1/2})}{2h} & \frac{f'(q_N)}{2} \end{pmatrix}. \quad (\text{A4})$$

For stability, $f'(x)$ should be negative. If $f'(x)$ is bounded and N is large, the diagonal terms are negligible. In this case, one may simulate only the anti-Hermitian part $\frac{A-A^\dagger}{2}$ and approximate the dynamics by unitary evolution.

2. Upwind scheme

For hyperbolic PDEs, the dynamics are typically asymmetric, and the use of centered differences is often unstable. An alternative approach with better stability is the upwind scheme, where a one-sided approximation to the derivative is used. This also enables the use of non-periodic boundary conditions, i.e. an inflow boundary. Note that the outflow boundary is already determined and an additional constraint cannot be imposed [66]. Here, we assume the inflow boundary condition $u_1 = 0$ with coefficient function $f(x) > 0$. The upwind scheme in this case corresponds to the discretization of (A1) by

$$\frac{du_j}{dt} = -f(q_j) \left(\frac{u_j - u_{j-1}}{h} \right). \quad (\text{A5})$$

This corresponds to (A2) with coefficient matrix

$$A_u = \begin{pmatrix} -\frac{f(q_1)}{h} & & & \\ \frac{f(q_2)}{h} & -\frac{f(q_2)}{h} & & \\ & \ddots & \ddots & \\ & & \ddots & \ddots \\ & & & \frac{f(q_N)}{h} & -\frac{f(q_N)}{h} \end{pmatrix}. \quad (\text{A6})$$

Since $f(x) > 0$, the eigenvalues of $\frac{A_u+A_u^\dagger}{2}$ are non-positive and thus the system is stable. In the case when $f(x) < 0$, one should instead approximate $\frac{\partial u(t, x_j)}{\partial x}$ by $\frac{u_{j+1} - u_j}{h}$.

Appendix B: Hamiltonian embeddings of sparse matrices

In this section, we review Hamiltonian embedding, a recently proposed framework that enables the simulation of sparse Hamiltonians [34]. For simulating partial differential equations, we focus on encoding schemes that allow for efficient embeddings of banded and circulant banded matrices, which arise from finite difference discretizations of differential operators.

To simulate a sparse matrix A , the Hamiltonian embedding technique makes use of an embedding Hamiltonian H_A whose projection onto a subspace \mathcal{S} precisely matches A . That is, with respect to the subspaces \mathcal{S} and \mathcal{S}^\perp , H_A can be written as a block matrix

$$H_A = \begin{pmatrix} A & R^\dagger \\ R & G \end{pmatrix}, \quad (\text{B1})$$

where $A = P_S H_A P_S$, $G = P_{S^\perp} H_A P_{S^\perp}$, $R = P_{S^\perp} H_A P_S$, and P_S and P_{S^\perp} are projectors onto \mathcal{S} and \mathcal{S}^\perp , respectively.

In the case when $\|R\| > 0$, it was shown in [34] that a sufficiently large penalty Hamiltonian may be used to control the simulation error. However, the simulation of H_A using usual product formulas leads to large simulation error when the penalty coefficient is large. To overcome this limitation, here we consider penalty-free versions of the one-hot, unary, and circulant unary embeddings which lead to improved asymptotic complexity using standard product formulas.

In this section, we index bitstrings starting from 1 and denote bitstrings from right to left, e.g. the first bit of 001 is 1. We use X_j , Y_j , and Z_j to denote Pauli matrices

$$X = \begin{pmatrix} 0 & 1 \\ 1 & 0 \end{pmatrix}, \quad Y = \begin{pmatrix} 0 & -i \\ i & 0 \end{pmatrix}, \quad Z = \begin{pmatrix} 1 & 0 \\ 0 & -1 \end{pmatrix}$$

applied to the j -th qubit, respectively. Furthermore, we make extensive use of the number operator $\hat{n}_j^{(1)} = \frac{I - Z_j}{2}$ and its orthogonal complement $\hat{n}_j^{(0)} = \frac{I + Z_j}{2}$ on the j -th qubit. For a matrix A , we denote its (j, k) entry by $A_{j,k}$ if $j \neq k$ or A_j if $j = k$.

1. Penalty-free embedding schemes

One-hot embedding

For simulating partial differential equations on digital quantum computers, the one-hot embedding without penalty offers both simplicity and flexibility due to the use of only 2-local operators.

Definition 2 (One-hot code). The one-hot code consists of bitstrings $\{h_1, \dots, h_n\}$ such that for $j = 1, \dots, N$, h_j is the bitstring of length N whose j -th bit is 1 and all other bits are 0.

Proposition 1 (One-hot embedding without penalty). *Let $A \in \mathbb{C}^{N \times N}$ be a Hermitian matrix. Let \mathcal{S} be the subspace spanned by the set of one-hot states $\{|h_j\rangle \mid j = 1, \dots, N\}$. Then the Hamiltonian*

$$H_A = \frac{1}{2} \left(\sum_{j < k} \text{Re}(A_{j,k})(X_k \otimes X_j + Y_k \otimes Y_j) + \text{Im}(A_{j,k})(X_k \otimes Y_j - Y_k \otimes X_j) \right) + \left(\sum_{j=1}^N A_j \hat{n}_j^{(1)} \right) \quad (\text{B2})$$

satisfies $H_A|_{\mathcal{S}} = A$ and \mathcal{S} is an invariant subspace of H_A .

Unary embedding

In the case of non-periodic boundary conditions, the finite difference operators are banded matrices, where the (j, k) entries are nonzero only if $|j - k| \leq b$ for an integer bandwidth $b \geq 0$. In this case, the unary embedding provides an alternative to the one-hot code.

Definition 3 (Unary code). The unary embedding consists of bitstrings $\{u_1, \dots, u_N\}$ of length $(N - 1)$ such that for $j = 1, \dots, N$, the first $(j - 1)$ bits of u_j are 1's and remaining $(N - j)$ bits are 0's.

Penalty-free embeddings of band matrices with arbitrary bandwidth may be constructed using the unary code. However, the penalty-free version require increased locality and in general consists of a number of Pauli terms which is exponential in the bandwidth. Therefore, for simplicity, we consider the penalty-free unary embedding of a tridiagonal matrix as follows.

Proposition 2 (Unary embedding without penalty). *Let $A \in \mathbb{C}^{N \times N}$ be a Hermitian, tridiagonal matrix. Let \mathcal{S} be the subspace spanned by the set of unary states $\{|u_j\rangle \mid j = 1, \dots, N\}$. Then the Hamiltonian*

$$\begin{aligned} H_A = & \hat{n}_2^{(0)} (\text{Re}(A_{1,2})X_1 - \text{Im}(A_{1,2})Y_1) + \left(\sum_{j=2}^{N-1} \hat{n}_{j+1}^{(0)} (\text{Re}(A_{j,j+1})X_j - \text{Im}(A_{j,j+1})Y_j) \hat{n}_{j-1}^{(1)} \right) \\ & + (\text{Re}(A_{N-1,N})X_N - \text{Im}(A_{N-1,N})Y_N) \hat{n}_{N-1}^{(1)} + \left(A_{1,1}I + \sum_{j=2}^N (A_j - A_{j-1}) \hat{n}_{j-1}^{(1)} \right) \end{aligned} \quad (\text{B3})$$

satisfies $H_A|_{\mathcal{S}} = A$ and \mathcal{S} is an invariant subspace of H_A .

Remark 2. The unary embedding is equivalent to the one-hot embedding in the following sense. For any unary state $|u_j\rangle$, we can introduce an additional ancilla qubit initialized to $|1\rangle$ and perform a ladder of CNOT gates:

$$\left(\prod_{j=2}^N CX_{j,j-1} \right) |u_j\rangle |1\rangle = |h_j\rangle. \quad (\text{B4})$$

Consequently, any $(N-1)$ -qubit state $\sum_{j=1}^N \alpha_j |u_j\rangle$ in the unary embedding subspace can be mapped to the N -qubit one-hot embedded state $\sum_{j=1}^N \alpha_j |h_j\rangle$ in depth $\mathcal{O}(N)$, and vice-versa. With mid-circuit measurement and feedforward, the CNOT ladder can be implemented in $\mathcal{O}(1)$ depth [67].

Circulant unary embedding

For matrices with cyclic structure (arising from the use of periodic boundary condition), the circulant unary embedding may be used.

Definition 4 (Circulant unary code). Let N be an even integer. The circulant unary code consists of bitstrings $\{c_1, \dots, c_N\}$ of length $N/2$ such that

- if $j = 1, \dots, N/2$, the first $(j-1)$ bits of c_j are 1's and the remaining $(N+1-j)$ are 0's;
- if $j = N/2+1, \dots, N$, c_j is the bitwise complement of $c_{j-N/2}$.

Similar to the unary embedding, we consider the penalty-free circulant unary embedding of a tridiagonal matrix as follows.

Proposition 3 (Circulant unary embedding without penalty). Let $A \in \mathbb{C}^{N \times N}$ be a Hermitian, tridiagonal matrix. Let \mathcal{S} be the subspace spanned by the set of circulant unary states $\{|c_j\rangle \mid j = 1, \dots, N\}$. For $j = 1, \dots, N$, define a_j , b_j , and c_j as follows:

$$a_j = \begin{cases} 1 & \text{if } N/2-1 \leq j < N, \\ 0 & \text{otherwise,} \end{cases} \quad b_j = \begin{cases} 1 & \text{if } 1 < j \leq N/2, \\ 0 & \text{otherwise,} \end{cases} \quad c_j = \begin{cases} 1 & \text{if } j \geq N/2, \\ 0 & \text{otherwise.} \end{cases}$$

Then the Hamiltonian

$$H_A = \sum_{j=1}^N \hat{n}_{j+1}^{(a_j)} (\text{Re}(A_{j,j+1})) X_j + (-1)^{c_j} \text{Im}(A_{j,j+1}) Y_j \hat{n}_{j-1}^{(b_j)} + A_j \hat{n}_j^{(c_j)} \hat{n}_{j-1}^{(b_j)} \quad (\text{B5})$$

(where indices are taken modulo $N/2$) satisfies $H_A|_{\mathcal{S}} = A$ and \mathcal{S} is an invariant subspace of H_A .

Both Proposition 2 and Proposition 3 are proved via straightforward calculation, as the operators involving $A_{j,j+1}$ only act nontrivially on the j -th and $(j+1)$ -th codewords.

Appendix C: Standard binary encodings of sparse matrices

1. Polynomial functions

The standard binary encoding enables a compact representation of diagonal operators corresponding to polynomial functions of a real variable. Here, we use n qubits to represent a real-variable $x \in [0, 1]$ and discretize the interval by $N = 2^n$ grid points. For a variable y defined on a more general interval $[L, R]$, one may rescale and translate x via $y = (R - L)x - L$.

Proposition 4. Let $N = 2^n$ for $n \geq 1$. Let $P = \text{diag}(0, 1, \dots, N-1)/N$. Then the Pauli decomposition of P is

$$P = \frac{1}{2N} \left((N-1)I - \sum_{j=1}^n 2^{j-1} Z_j \right) \quad (\text{C1})$$

Proof. For any computational basis state $|k\rangle$, let $q_i \in \{0, 1\}$ be the value of the i -th bit. Then $k = \sum_{i=1}^n 2^{i-1} q_i$. Then,

$$\langle k | \sum_{j=1}^n 2^{j-1} Z_j | k \rangle = \sum_{j=1}^n 2^{j-1} (1 - 2q_j) = 2^n - 1 - 2k. \quad (\text{C2})$$

Therefore,

$$\frac{k}{N} = \frac{1}{2N} \langle k | \left(2^n - 1 - \sum_{j=1}^n 2^{j-1} Z_j \right) | k \rangle = \langle k | P | k \rangle. \quad (\text{C3})$$

□

Remark 3. It immediately follows that a general polynomial $\sum_{k=0}^K a_k x^k$ may be encoded by the operator $\sum_{k=0}^K a_k P^k$. As a consequence, the locality of the operator corresponds to the degree of the polynomial and the number of Pauli terms may be as large as N for the standard binary code. In contrast, the one-hot code requires N single-qubit operators, regardless of the degree K . An empirical comparison of the standard binary code and one-hot code for simulating diagonal operators is shown in Fig. 5.

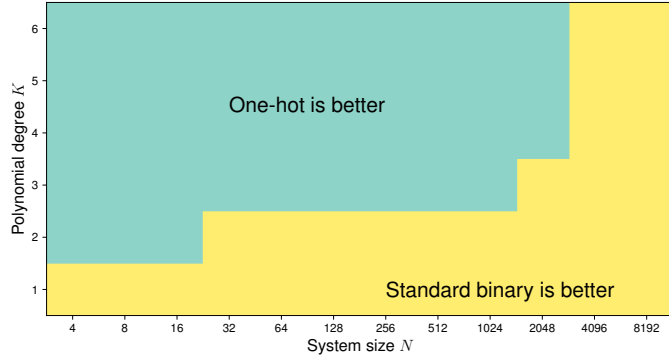


FIG. 5. Landscape of the best encoding scheme for simulating a diagonal operator P^K for varying system size N and polynomial degree K , determined by the total number of 1- and 2-qubit gates. The yellow region shows the regime where standard binary uses fewer gates, while the teal region shows where the one-hot code uses fewer gates. For linear polynomials, the standard binary code outperforms the one-hot code for system size up to $N = 256$. For higher degree polynomials, the one-hot code tends to use fewer gates, unless the system size is very large.

In particular, the standard binary encoding allows for a highly efficient decomposition of diagonal matrices containing Fourier frequencies. For consistency with the QFT, we let the first entry be the zero-frequency component, unlike in Proposition 4.

Proposition 5. Let $N = 2^n$ for $n \geq 1$. Let $H_d = \text{diag}(0, 1, \dots, N/2 - 1, -N/2, -N/2 + 1, \dots, -1)$. Then the Pauli decomposition of H_d is

$$H_d = -\frac{1}{2} \left(I - 2^n Z_n + \sum_{j=1}^n 2^{j-1} Z_j \right). \quad (\text{C4})$$

Proof. Similar to the proof of Proposition 4, we have

$$\langle k | \sum_{j=1}^n 2^{j-1} Z_j | k \rangle = 2^n - 1 - 2k, \quad (\text{C5})$$

where $|k\rangle$ denotes the standard binary encoding of k . Then by straightforward calculation,

$$\langle k | H_d | k \rangle = \begin{cases} k & \text{if } k \leq N/2 - 1, \\ k - N & \text{if } k \geq N/2. \end{cases} \quad (\text{C6})$$

□

2. Finite difference operators

Here, we discuss the standard binary encoding of finite difference operators and how this approach compares to sparse encodings such as the one-hot or unary codes. We consider tridiagonal matrices of the form

$$A = \sum_{j=0}^{N-1} a_j |j+1\rangle\langle j| + a_j^* |j\rangle\langle j+1|, \quad (\text{C7})$$

which includes discretizations of both first and second-order differential operators, with or without periodic boundary conditions.

In the special case of homogeneous entries (i.e. $a_j = a$ for all j), circuit implementations for simulating (C7) were proposed in [13]. These circuit constructions were subsequently utilized for simulating non-unitary dynamics via Schrödingerization in [44]. Strictly speaking, this approach represents the finite difference operators using the standard binary encoding. In general, the standard binary encoding for an N -point finite difference operator requires $\mathcal{O}(N)$ of Pauli terms despite using only $\mathcal{O}(\log N)$ qubits (see [68] for the Pauli decomposition of general tridiagonal matrices). However, [13] circumvents the naive implementation by decomposing and simulating each term in the operator using the so-called Bell basis rather than the Pauli basis. This approach offers an efficient implementation with only $\mathcal{O}(\log N)$ space and $\mathcal{O}(\text{poly log } N)$ gates per Trotter step, but suffers from two major disadvantages.

- First, the constructed circuits are only applicable to tridiagonal matrices with homogeneous entries. When considering differential equations with variable coefficients, the entries are generally inhomogeneous and must be represented by $\mathcal{O}(N)$ parameters. In these cases, dense encodings such as the standard binary code may save space, but cannot achieve $\mathcal{O}(\text{poly log } N)$ gates per Trotter step without further leveraging the problem structure.

In the case of inhomogeneous entries, it is possible to simulate $a_j |j\rangle\langle j+1| + a_j^* |j\rangle\langle j|$ for each j by applying increment and decrement operators (see for example [69]) and simulating $(|0\rangle\langle 1|)^{\otimes n} + (|1\rangle\langle 0|)^{\otimes n}$ via the circuits from [13]. Using this approach, the Trotter error is the same as one-hot or unary encodings. However, since this must be done for all $j = 1, \dots, N$, the overall gate complexity is $\mathcal{O}(N \cdot \text{poly log } N) = \tilde{\mathcal{O}}(N)$. This is worse than sparse encodings such as one-hot or unary only by logarithmic factors.

- Second, the standard binary code requires highly non-local operators. As a result, the circuit implementation of these finite difference operators requires decomposing multi-controlled rotation operators and may lead to high overhead in practice. The actual costs of such decompositions depends largely on the device architecture.

It is also worth noting that even in the case of homogeneous entries, the use of the standard binary code for simulating partial differential equations is not exponentially more efficient than sparse encodings such as the one-hot or unary codes. The use of finite differences leads to a factor of $1/h = \mathcal{O}(N)$ in the Hamiltonian, so the Trotter number scales at least linearly in N . At best, the standard binary code achieves a gate complexity that is only a linear factor of N better than the one-hot or unary codes when simulating finite difference operators.

Appendix D: Quantum simulation of non-unitary dynamics

We review two complementary methods for solving (1) in the general case when $A(t)$ is not necessarily anti-Hermitian. This includes linear combination of Hamiltonian simulation (LCHS) [28, 70] and Schrödingerization [27], which are distinct yet closely related methods for mapping non-unitary dynamics to unitary dynamics. We apply each of these methods in conjunction with Hamiltonian embedding to obtain resource-efficient algorithms for simulating non-unitary dynamics.

1. Linear combination of Hamiltonian simulation

The original work on LCHS [28] establishes the following identity:

$$\mathcal{T}e^{\int_0^t A(s) ds} = \int_{\mathbb{R}} \frac{1}{\pi(1+k^2)} \mathcal{T}e^{i \int_0^t k H_1(s) + H_2(s) ds} dk. \quad (\text{D1})$$

where $H_1(t) = \frac{A(t) + A(t)^\dagger}{2}$ and $H_2(t) = \frac{A(t) - A(t)^\dagger}{2i}$, assuming $H_1(t) \preceq 0$ for stability.

In [70], this formula was generalized by replacing the integrand $\frac{1}{\pi(1+k^2)}$ by a large family of functions to obtain a quantum algorithm with near-optimal dependence on all parameters for solving (1). The general formula is given by

$$\mathcal{T}e^{\int_0^t A(s) ds} = \int_{\mathbb{R}} \frac{f(k)}{1-ik} \mathcal{T}e^{i \int_0^t k H_1(s) + H_2(s) ds} dk, \quad (\text{D2})$$

where the kernel function $f(k)$ satisfies mild analyticity, decay, and normalization conditions [70, Theorem 5]. The integration in (D2) is truncated to a finite interval $[-R, R]$ and approximated by a finite sum:

$$\begin{aligned} \mathcal{T}e^{\int_0^t A(s) ds} &\approx \int_{-R}^R \frac{f(k)}{1-ik} \mathcal{T}e^{i \int_0^t k H_1(s) + H_2(s) ds} dk \\ &\approx \sum_{j=0}^{M-1} c_j U_j(t), \end{aligned} \quad (\text{D3})$$

where $U_j(t) = \mathcal{T}e^{i \int_0^t k_j H_1(s) + H_2(s) ds}$. The weights c_j 's and quadrature points k_j 's depend on the chosen numerical integration scheme.

An observable $u(t)^\dagger O u(t)$ can be approximated by

$$u(t)^\dagger O u(t) \approx \sum_{j_1, j_2} c_{j_1}^* c_{j_2} u(t)^\dagger U_{j_1}^\dagger(t) O U_{j_2}(t) u(t). \quad (\text{D4})$$

This observable can be computed by Monte Carlo sampling pairs (j_1, j_2) with probability proportional to $c_{j_1}^* c_{j_2}$ and evaluating each correlation function $u(0)^\dagger U_{j_1}^\dagger(t) O U_{j_2}(t) u(0)$ on a quantum computer via the Hadamard test [71].

The choice of the truncation parameter R required to approximate the integral in (D2) with precision ϵ depends on the choice of $f(k)$. The original LCHS formula (D1), which is obtained from setting $f(k) = \frac{1}{\pi(1+ik)}$, requires $K = \mathcal{O}(\frac{1}{\epsilon})$. Using the improved kernel function $f(z) = \frac{1}{2\pi e^{-2\beta} e^{(1+iz)^\beta}}$ for $\beta \in (0, 1)$, the cutoff can be chosen as $K = \mathcal{O}((\log(1/\epsilon))^{1/\beta})$.

We summarize the steps for implementing the hybrid LCHS algorithm in Algorithm 2.

Algorithm 2: Hybrid LCHS

Input: Hamiltonian embeddings $\tilde{H}_1, \tilde{H}_2, \tilde{O}$, encoded initial state \tilde{u}_0 , evolution time t , number of samples N_{samples} .
Output: Estimate of observable $u(T)^\dagger O u(T)$.

- 1 **for** $i = 1, \dots, N_{\text{samples}}$ **do**
- 2 Randomly sample pairs (j_1, j_2) with probability proportional to $c_{j_1}^* c_{j_2}$, where c_j 's are weights as in (D3).
- 3 Apply the Hadamard test to estimate the correlation function $\tilde{u}(0)^\dagger U_{j_1}^\dagger(T) \tilde{O} U_{j_2}(T) \tilde{u}(0)$, where
 $U_{j_1}(T) = e^{it(k_{j_1} \tilde{H}_1 + \tilde{H}_2)}$ and $U_{j_2}(T) = e^{it(k_{j_2} \tilde{H}_1 + \tilde{H}_2)}$.
- 4 Estimate $u(T)^\dagger O u(T) = \tilde{u}(T)^\dagger \tilde{O} \tilde{u}(T)$ by averaging the values according to (D4).

2. Schrödingerization

The recently proposed method known as Schrödingerization [27] maps the linear ODE in (1) to the Schrödinger equation, for which the dynamics are unitary. This procedure makes use of the warped phase transformation, in which one defines an auxiliary variable p and the mapping $v(t, p) = e^{-p} u(t)$ for $p > 0$. Rather than directly solving (1), one instead solves the linear convection equation

$$\begin{aligned} \frac{\partial}{\partial t} v(t, p) &= -H_1(t) \frac{\partial}{\partial p} v(t, p) + i H_2(t) v(t, p) \\ v(0, p) &= e^{-|p|} u_0, \end{aligned} \quad (\text{D5})$$

where $H_1(t)$ and $H_2(t)$ are the real and imaginary parts of $A(t)$ given by the Cartesian decomposition $A(t) = H_1(t) + i H_2(t)$.

The linear operator in (D5) is anti-self-adjoint. As a result, (D5) is a special case of the Schrödinger equation and can be solved using standard Hamiltonian simulation techniques. Then the solution to (1) can be recovered by integrating out the auxiliary variable:

$$u(T) = \int_0^\infty v(T, p) dp. \quad (\text{D6})$$

In practice, an observable of the form $u(T)^\dagger O u(T)$ is computed by post-selecting measurements for which $p > 0$ and computing the expectation value of O on the system register normally.

We summarize the steps for implementing Schrödingerization in Algorithm 3.

Algorithm 3: Schrödingerization

Input: Hamiltonian embeddings $\tilde{H}_1, \tilde{H}_2, \tilde{O}$, encoded initial state \tilde{u}_0 , evolution time T , number of auxiliary qubits n_p .

Output: Estimate of observable $u(T)^\dagger O u(T)$.

- 1 Using an n_p -qubit register to represent p , prepare the initial state $|\Psi_{\text{Laplace}}\rangle$ with amplitudes proportional to the Laplace distribution.
- 2 Apply the QFT to the p -register.
- 3 Simulate $\tilde{H}_1 \otimes H_F - \tilde{H}_2 \otimes I$ for time T , where H_F is the diagonal matrix of Fourier frequencies.
- 4 Apply the inverse QFT to the p -register.
- 5 Estimate $u(T)^\dagger O u(T)$ via observable measurements and post-selection.

3. Proof of Schrödingerization

LCHS and Schrödingerization accomplish exactly the same task of solving (1). In fact, we remark that LCHS and Schrödingerization are mathematically equivalent, as both are based upon the LCHS formula (D1).

Theorem 2. *Let $u(t)$ be the solution to the linear ODE in (1) and let $v(t, p)$ be the solution to the PDE (D5). Then $u(t) = \int_0^\infty v(t, p) dp$.*

Proof. Applying the Fourier transform to $v(t, p)$ with respect to p yields

$$\hat{v}(t, k) = \frac{1}{\sqrt{2\pi}} \int_{\mathbb{R}} e^{ipk} v(t, p) dp. \quad (\text{D7})$$

Then (D5) becomes

$$\frac{\partial}{\partial t} \hat{v}(t, k) = i(kH_1(t) + H_2(t)) \hat{v}(t, k), \quad (\text{D8})$$

with initial condition $\hat{v}(0, k) = \frac{\sqrt{2/\pi}}{k^2 + 1} u_0$. The Schrödinger equation (D8) has solution

$$\hat{v}(x, k) = \mathcal{T} e^{i \int_0^x (kH_1(s) + H_2(s)) ds} \frac{\sqrt{2/\pi}}{k^2 + 1} u_0. \quad (\text{D9})$$

The solution to the original PDE $v(t, p)$ is recovered by taking the inverse Fourier transform:

$$v(t, p) = \frac{1}{\sqrt{2\pi}} \int_{\mathbb{R}} e^{-ipk} \hat{v}(t, k) dk u_0 \quad (\text{D10})$$

$$= \frac{1}{\sqrt{2\pi}} \int_{\mathbb{R}} e^{-ipk} \mathcal{T} e^{i \int_0^t (kH_1(s) + H_2(s)) ds} \frac{\sqrt{2/\pi}}{k^2 + 1} dk u_0 \quad (\text{D11})$$

$$= \int_{\mathbb{R}} \mathcal{T} e^{i \int_0^t (k(H_1(s) - p/t) + H_2(s)) ds} \frac{1}{\pi(k^2 + 1)} dk u_0. \quad (\text{D12})$$

Since $H_1 \preccurlyeq 0$, $H_1 - p/t$ is negative if $p \geq 0$. Using [28, Theorem 1], we have

$$v(t, p) = e^{-p} \mathcal{T} e^{\int_0^t A(s) ds} u_0 = e^{-p} u(t), \quad p \geq 0. \quad (\text{D13})$$

Thus, we have $u(t) = \int_0^\infty v(t, p) dp$ since $\int_0^\infty e^{-p} dp = 1$. \square

Remark 4. Schrödingerization can be generalized by choosing the initial state to be the Fourier transform of any valid kernel function in [70]. The proof of correctness is nearly identical, with the only difference being the initial function. Compared to the original integrand $\frac{1}{\pi(1+\eta^2)}$, these kernel functions have better decay properties that enable a smaller truncation interval in the asymptotic regime. In Appendix D 4, we show a straightforward protocol for preparing the Laplace distribution. However, our proof of Theorem 3 depends on the use of the improved kernel functions and assumes an efficient protocol for preparing them as a quantum state.

4. Implementation of Schrödingerization

In this section, we discuss details of the end-to-end implementation of Schrödingerization. The overall implementation consists of three components: (1) initial state preparation, (2) quantum simulation of the linear convection equation in (D5), as well as (3) measurement of observables.

The overall quantum circuit is shown in Fig. 2. We use two quantum registers: one for p and one for u . We use the standard binary code with n_p qubits for p , while the encoding for u largely depends on the target application. The quantum state proportional to the discretized solution to (D5) is denoted as $|v(t, p)\rangle$.

To represent the p variable in a quantum register, we first truncate the real space to the interval $[-R, R]$. Note that the endpoint R should be chosen to scale as $\mathcal{O}(\|H_1\|t)$ since the wave function travels in the negative p direction at a rate proportional to $\|H_1\|t$. Next, we discretize with $N_p = 2^{n_p}$ grid points p_0, \dots, p_{N_p-1} such that $p_k = -R + k\Delta p$, where $\Delta p = \frac{2R}{N_p-1}$. For $j = 0, \dots, N_p - 1$, we use $|j\rangle$ to represent the point p_j , where $|j\rangle$ denotes the standard binary representation of j .

a. Initial state preparation. The first step of Schrödingerization is the task of initial state preparation of the Laplace distribution. As the initial condition of (D5) is $v(0, p) = e^{-|p|}u_0$, we must prepare an n_p -qubit quantum state whose amplitudes are proportional to the Laplace distribution $f(p) = e^{-|p|}$, $p \in \mathbb{R}$. Here, we resolve this initialization issue, which to our knowledge has not been fully addressed in previous literature.

In what follows, we omit the implicit normalization factor for simplicity. This normalization factor does not appear when computing observables. Formally, the goal is to approximate the quantum state $|\psi_{\text{Laplace}}\rangle = \sum_{j=0}^{N_p-1} e^{-|p_j|} |j\rangle$.

To construct a circuit for the Laplace distribution, we first consider the right half of the real line, i.e. the exponential distribution e^{-p} for $p \geq 0$. We start by showing how one may prepare an n -qubit state $|\psi_{\text{Exp},n}\rangle = \sum_{j=0}^{2^n-1} e^{-|q_j|} |j\rangle$, where $q_j = jh$ and $h = \frac{R}{2^n}$.

A key observation is that $|\psi_{\text{Exp},n}\rangle$ is a product state:

$$|\psi_{\text{Exp},n}\rangle = \bigotimes_{i=0}^{n-1} \left(|0\rangle + e^{-2^{n-1-i}h} |1\rangle \right). \quad (\text{D14})$$

For each $i = 0, \dots, n-1$, the single-qubit state $(|0\rangle + e^{-2^{n-1-i}h} |1\rangle)$ is readily prepared using a single Pauli- y rotation with angle $\theta_i = 2 \arccos\left(\frac{1}{\sqrt{1+e^{-2(2^{n-1-i}h)}}}\right)$. Thus $|\psi_{\text{Exp},n}\rangle$ can be prepared by a single layer of Pauli- y rotations.

To prepare the Laplace distribution on n_p qubits, we start with an (n_p-1) -qubit state $|\psi_{\text{Exp},n_p-1}\rangle$ for the exponential distribution. We introduce an additional qubit as the most significant bit. Let q_0, \dots, q_{n_p-1} denote the qubits where q_{n_p-1} is the newly introduced most significant bit. We symmetrize the distribution with a Hadamard gate on q_{n_p-1} , followed by a sequence of n_p-1 CNOT gates each controlled on q_{n_p-1} and targeting q_i for $i = 0, \dots, n_p-2$, followed by an X gate on q_{n_p-1} . The full state preparation circuit is shown in Fig. 6.

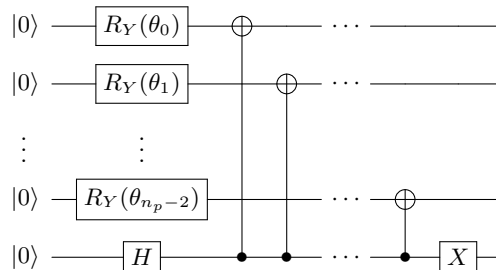


FIG. 6. Quantum circuit for preparing the Laplace distribution.

b. Hamiltonian simulation. Next, we discuss the simulation of the linear convection equation given by (D5). When mapped to the Schrödinger equation, the Hamiltonian to simulate is given as $-iH_1(t)\partial_p - H_2(t)$ (before discretization of p). To implement $-i\partial_p$, we enforce periodic boundary conditions and apply the Fourier spectral method to the auxiliary variable p . By Proposition 5, the matrix of Fourier frequencies is given by a sum of 1-local Pauli- z operators:

$$H_{\mathcal{F}} = -\frac{\pi}{2R} \left(I - 2^{n_p} Z_{n_p} + \sum_{j=1}^{n_p} 2^{j-1} Z_j \right). \quad (\text{D15})$$

Upon applying Hamiltonian embedding, H_1 and H_2 are mapped to \tilde{H}_1 and \tilde{H}_2 , respectively. Then, the overall embedding Hamiltonian to simulate is given by

$$\tilde{H}_S = \tilde{H}_1 \otimes H_{\mathcal{F}} - \tilde{H}_2 \otimes I, \quad (\text{D16})$$

which can be simulated using standard methods for sparse Hamiltonian simulation (e.g., product formulas). Finally, an application of the inverse QFT is applied to the p -register to obtain

$$|\psi(t)\rangle = (I \otimes \mathcal{F}^{-1}) e^{-itH_S} (I \otimes \mathcal{F}) (|u_0\rangle \otimes |\psi_{\text{Laplace}}\rangle), \quad (\text{D17})$$

where \mathcal{F} denotes the quantum Fourier transform.

c. Measurement of observables. The final step of Schrödingerization is to recover the solution $u(t)$ by integrating out the auxiliary variable according to (D6). Since $v(t, p) = e^{-p}u(t)$ for $p > 0$, we have

$$u(t)^\dagger O u(t) = 2 \int_0^\infty v(t, p)^\dagger O v(t, p) dp. \quad (\text{D18})$$

Thus, observables of the form $u(t)^\dagger O u(t)$ may be computed by measuring the p -register and post-selecting for values of $p > 0$, obtaining the unnormalized state

$$\rho_u = \sum_{k=N_p/2}^{N_p-1} (I \otimes \langle k |) |\psi(t)\rangle \langle \psi(t) | (I \otimes |k\rangle). \quad (\text{D19})$$

Note that this is not a partial trace operation and ρ_u is not a density operator, since $\text{Tr } \rho_u < 1$. Finally, the observable is estimated by

$$u(t)^\dagger O u(t) \approx 2 \text{Tr}(O \rho_u). \quad (\text{D20})$$

Appendix E: Quantum ODE solvers using Hamiltonian embedding

1. Hamiltonian simulation via product formulas and Richardson extrapolation

Our description of LCHS and Schrödingerization thus far have not specified the method for performing Hamiltonian simulation. In this work, we consider the use of product formulas combined with Richardson extrapolation, which enables us to achieve near-optimal complexity for simulating ODEs.

Given a Hamiltonian $H = \sum_{\gamma=1}^{\Upsilon} H_\gamma$, an Υ -stage product formula \mathcal{P} is given by [72]

$$\mathcal{P}(t) := \prod_{v=1}^{\Upsilon} \prod_{\gamma=1}^{\Gamma} e^{-ita_{(v,\gamma)} H_{\pi_v(\gamma)}}, \quad (\text{E1})$$

where Υ is the number of stages. For a $2k$ -th order Trotter-Suzuki formula, the number of stages is $\Upsilon = 2 \cdot 5^{k-1}$. For a given product formula \mathcal{P} , the symmetry class σ is 2 if \mathcal{P} is symmetric (i.e. $\mathcal{P}(-t) = \mathcal{P}^{-1}(t)$), or 1 otherwise. Throughout this section, we also let $a_{\max} = \max_{v,\gamma} |a_{(v,\gamma)}|$.

We use the notation $[X_1 X_2 \dots X_n]$ to denote the right-nested commutators:

$$[X_1 X_2 \dots X_n] := [X_1, [X_2, [\dots, [X_{n-1}, X_n]]]], \quad (\text{E2})$$

and define

$$\alpha_{\text{comm}}^{(j)} := \sum_{\gamma_1, \dots, \gamma_j=1}^{\Gamma} \|[H_{\gamma_1} H_{\gamma_2} \dots H_{\gamma_j}]\|. \quad (\text{E3})$$

It has been shown that the error of a p -th order staged product formula has commutator scaling [72]:

$$\|e^{-tiH} - \mathcal{P}(t)\| = \mathcal{O}(\alpha_{\text{comm}}^{(p+1)} t^{p+1}) \quad (\text{E4})$$

for small t .

The direct application of product formulas to simulate long-time evolution with accuracy ϵ results in runtime the scales polynomially in $1/\epsilon$. In [59], it was shown that the dependence on ϵ can be improved to $\log(1/\epsilon)$ using classical post-processing in the form of Richardson extrapolation.

Proposition 6 (Richardson extrapolation, [59]). *Let $f : [-1, 1] \rightarrow \mathbb{R}$ have the series expansion*

$$f(s) = f(0) + \sum_{j=1}^{\infty} c_j s^j. \quad (\text{E5})$$

Let $s_0 > 0$ and choose extrapolation nodes $s_i = s_0/r_i$ for integers r_1, \dots, r_m . Then by choosing coefficients b_k appropriately, the Richardson extrapolation

$$F^{(m)}(s_0) = \sum_{k=1}^m b_k f(s_0/r_k) \quad (\text{E6})$$

satisfies

$$|F^{(m)}(s_0) - f(0)| = \mathcal{O}(s_0^{m+1}). \quad (\text{E7})$$

Remark 5. The conditioning of the extrapolation depends on the choice of extrapolation nodes, which affects the 1-norm of the coefficients b_j . In particular, one may choose

$$r_k = r_{\text{scale}} \left\lceil \frac{\sqrt{8m}}{\pi \sin(\pi(2k-1)/8m)} \right\rceil, \quad (\text{E8})$$

which gives $\|b\|_1 = \mathcal{O}(\log m)$ [59].

In the context of Hamiltonian simulation, we define

$$f(s) = \langle O_s \rangle := \text{Tr} \left(O \mathcal{P}(sT)^{1/s} \rho_0 (\mathcal{P}(sT)^{1/s})^\dagger \right), \quad (\text{E9})$$

where $s > 0$ represents the inverse Trotter number. We are interested in the zero step size limit, for which $\lim_{s \rightarrow 0} \langle O_s \rangle = \text{Tr} (O e^{-iT^H} \rho_0 e^{iT^H}) =: \langle O_0 \rangle$. For an m -term Richardson extrapolation, we evaluate the sequence of estimates $f(s_1), \dots, f(s_m)$ and use these values to estimate the expectation of the time-evolved observable $\langle O_0 \rangle$.

Lemma 1 (Trotter steps for Richardson extrapolation, [59, Corollary 4]). *Let $H = \sum_{\gamma=1}^{\Gamma} H_{\gamma}$ be a Hamiltonian, O be an observable, $T > 0$ be the evolution time, and ρ_0 be an initial state. Let \mathcal{P} be a symmetric p -th order Υ -stage product formula with symmetry class σ . Consider an m -term Richardson extrapolation (E6) for estimating $\langle O_0 \rangle := \text{Tr} (O e^{-iT^H} \rho_0 e^{iT^H})$ via the estimates $\langle O_{s_j} \rangle$ for $j = 1, \dots, m$. Assume s_1 is chosen such that $a_{\max} \Upsilon s_1 \lambda T < 1/2$ and r_{scale} is chosen large enough such that*

$$r_1 \geq (a_{\max} \Upsilon \lambda T)^{1 + \frac{1}{\sigma m} \lceil \frac{\sigma m}{p} \rceil} \left(\frac{4\|b\|_1}{\epsilon} \right)^{\frac{1}{\sigma m}}. \quad (\text{E10})$$

Then to estimate $\langle O_0 \rangle$ with error ϵ , the maximum number of Trotter steps in a single circuit is

$$\mathcal{O} \left((a_{\max} \Upsilon \lambda T)^{(1+1/p)} \log(1/\epsilon) \right), \quad (\text{E11})$$

where $a_{\max} = \max_{v, \gamma} a_{(v, \gamma)}$, and

$$\lambda := \sup_{\substack{j \in \sigma \mathbb{Z}_+ \geq \sigma m \\ 1 \leq l \leq K}} \left(\sum_{\substack{j_1, \dots, j_l \in \sigma \mathbb{Z}_+ \geq p \\ j_1 + \dots + j_l = j}} \prod_{\kappa=1}^l 2 \frac{\alpha_{\text{comm}}^{(j_{\kappa}+1)}}{(j_{\kappa}+1)^2} \right)^{1/(j+l)}. \quad (\text{E12})$$

Lemma 2 (Upper bound on λ for k -local Hamiltonians [73, Remark 3.2]). *Let $H = \sum_{j_1, \dots, j_k} H_{j_1, \dots, j_k}$ be a k -local Hamiltonian. Let*

$$\|H\|_1 = \max_{\ell} \left\{ \max_{j_{\ell}} \sum_{j_1, \dots, j_{\ell-1}, j_{\ell+1}, j_k} \|H_{j_1, \dots, j_k}\| \right\} \quad (\text{E13})$$

denote the induced 1-norm. Then, (E12) is upper bounded by

$$\lambda = \mathcal{O} \left(\left(\frac{\|H\|_1}{\|H\|_1} \right)^{1/p} \|H\|_1 \right). \quad (\text{E14})$$

2. Complexity analysis for Algorithm 1

We rigorously analyze the computational complexity for Algorithm 1 when using either LCHS or Schrodingerization to reduce the problem to Hamiltonian simulation. For the hybrid LCHS algorithm, each application of the Hadamard test can be viewed as simulating the Hamiltonian

$$H_{\text{LCHS}} = - \left(k_{j_1} \tilde{H}_1 \otimes |0\rangle\langle 0| + k_{j_2} \tilde{H}_1 \otimes |1\rangle\langle 1| + \tilde{H}_2 \otimes I \right), \quad (\text{E15})$$

where k_{j_1} and k_{j_2} are chosen randomly between $-R$ and R . Similarly, Schrödingerization requires the simulation of the Hamiltonian

$$H_S = \tilde{H}_1 \otimes H_{\mathcal{F}} - \tilde{H}_2 \otimes I \quad (\text{E16})$$

where $H_{\mathcal{F}}$ is a diagonal matrix of Fourier frequencies. Note that $\|H_{\mathcal{F}}\|_1 = \mathcal{O}(1/\Delta p)$ for step size Δp .

Lemma 3 (Upper bound on λ for LCHS and Schrodingerization). *Let H_1 and H_2 be Hamiltonians with Hamiltonian embeddings given by $\tilde{H}_1 = \sum_{\ell=1}^L \alpha_{\ell}^{(1)} P_{\ell}$ and $\tilde{H}_2 = \sum_{\ell=1}^L \alpha_{\ell}^{(2)} P_{\ell}$. Assume \tilde{H}_1 and \tilde{H}_2 are k -local, i.e., all P_{ℓ} act non-trivially on at most k qubits. Let H_{LCHS} and H_S be defined as in (E15) and (E16), respectively. Then when using a staged product formula \mathcal{P} to simulate either H_{LCHS} or H_S , the commutator scaling prefactor λ as defined in (E12) is given by*

$$\lambda_{\text{LCHS}} = \mathcal{O} \left((R\|\tilde{H}_1\|_1 + \|\tilde{H}_2\|_1)^{1/p} (R\|\tilde{H}_1\|_1 + \|\tilde{H}_2\|_1)^{1-1/p} \right) \quad (\text{E17})$$

for LCHS, and

$$\lambda_S = \mathcal{O} \left((\Delta p^{-1}\|\tilde{H}_1\|_1 + \|\tilde{H}_2\|_1)^{1/p} (\Delta p^{-1}\|\tilde{H}_1\|_1 + \|\tilde{H}_2\|_1)^{1-1/p} \right) \quad (\text{E18})$$

for Schrodingerization.

Proof. For LCHS,

$$\|H_{\text{LCHS}}\|_1 = \left\| - \left(\left(\frac{k_{j_1} + k_{j_2}}{2} \right) (\tilde{H}_1 \otimes Z) + \left(\frac{k_{j_1} - k_{j_2}}{2} \right) (\tilde{H}_1 \otimes Z) + \tilde{H}_2 \otimes I \right) \right\|_1 \quad (\text{E19})$$

$$\leq (R+1)\|\tilde{H}_1\|_1 + \|\tilde{H}_2\|_1 \quad (\text{E20})$$

$$= \mathcal{O} \left(R\|\tilde{H}_1\|_1 + \|\tilde{H}_2\|_1 \right). \quad (\text{E21})$$

For Schrödingerization,

$$\|H_S\|_1 = \left\| \tilde{H}_1 \otimes H_{\mathcal{F}} - \tilde{H}_2 \otimes I \right\|_1 \quad (\text{E22})$$

$$\leq \|\tilde{H}_1 \otimes H_{\mathcal{F}}\|_1 + \|\tilde{H}_2 \otimes I\|_1 \quad (\text{E23})$$

$$= \mathcal{O} \left(\frac{1}{\Delta p} \|\tilde{H}_1\|_1 + \|\tilde{H}_2\|_1 \right). \quad (\text{E24})$$

Similarly, we have $\|H_{\text{LCHS}}\|_1 = \mathcal{O} \left(R\|\tilde{H}_1\|_1 + \|\tilde{H}_2\|_1 \right)$ and $\|H_S\|_1 = \mathcal{O} \left(\Delta p^{-1}\|\tilde{H}_1\|_1 + \|\tilde{H}_2\|_1 \right)$ for the induced 1-norm. \square

Finally, our formal complexity analysis is given by Theorem 3.

Theorem 3. *Let H_1 and H_2 be Hamiltonians with Hamiltonian embeddings given by $\tilde{H}_1 = \sum_{\ell=1}^L \alpha_{\ell}^{(1)} P_{\ell}$ and $\tilde{H}_2 = \sum_{\ell=1}^L \alpha_{\ell}^{(2)} P_{\ell}$. Assume \tilde{H}_1 and \tilde{H}_2 are both k -local. Suppose we use either LCHS or Schrödingerization, along with a q -th order staged product formula and Richard extrapolation to estimate $u(T)^\dagger O u(T)$ with relative error ϵ . Then under the conditions of Lemma 1, the total number of 1- and 2-qubit gates per circuit is*

$$\mathcal{O} \left(k L \Upsilon^{2+o(1)} (a_{\max} T)^{1+o(1)} \log(1/\epsilon)^{3+o(1)} \left(\|\tilde{H}_1\|_1 + \|\tilde{H}_2\|_1 \right)^{o(1)} \left(\|\tilde{H}_1\|_1 + \|\tilde{H}_2\|_1 \right)^{1-o(1)} \right). \quad (\text{E25})$$

When using LCHS, the sample complexity (i.e., number of different circuits) required to estimate $u(T)^\dagger O u(T)$ with relative error ϵ with probability at least $1 - \delta$ is $\mathcal{O} \left(\frac{1}{\epsilon^2} \log \left(\frac{1}{\delta} \right) \right)$.

Proof. By Lemma 1, the maximum Trotter number required is $\mathcal{O} \left((a_{\max} \Upsilon \lambda T)^{(1+1/p)} \log(1/\epsilon) \right)$, where λ is the commutator scaling prefactor for either H_{LCHS} or H_S . We then bound λ using Lemma 3 for LCHS and Schrödingerization separately.

For LCHS, we have $\mathcal{O}(R) = \mathcal{O}((\log(1/\epsilon)^{1/\beta})$ by choosing the kernel function $f(k) = \frac{1}{2\pi e^{-2\beta} e^{(1+ik)\beta}}$, where $\beta \in (0, 1)$ [70]. For Schrödingerization, we have $\|H_S\| = \mathcal{O}(\Delta p^{-1})$. The discretization error from spectral methods depends on the smoothness of the initial function $v(0, p) = \psi(p)u_0$, where we choose $\psi(p)$ to be the Fourier transform of $f(k) = \frac{1}{2\pi e^{-2\beta} e^{(1+ik)\beta}}$. Since $f(k)$ decays exponentially fast, $\Delta p^{-1} = \mathcal{O}(\log(1/\epsilon))$ suffices. For more detailed analysis of Schrödingerization, we refer to [74, Section 4.1]. For generality, we bound the norm of H_{LCHS} and H_S by $\mathcal{O}((\log(1/\epsilon))^2)$. Thus,

$$\lambda = \mathcal{O} \left(\log(1/\epsilon)^2 \left(\|\tilde{H}_1\|_1 + \|\tilde{H}_2\|_1 \right)^{1/p} \left(\|\tilde{H}_1\|_1 + \|\tilde{H}_2\|_1 \right)^{1-1/p} \right) \quad (\text{E26})$$

For the gate complexity, an additional factor of $\mathcal{O}(kL\Upsilon)$ arises from exponentiating and decomposing each term, thereby yielding the claimed gate complexity.

To estimate $u(T)^\dagger O u(T)$ with absolute error ϵ , the sample complexity when using importance sampling is $\mathcal{O} \left(\frac{\|O\|^2}{\epsilon^2} \log \left(\frac{1}{\delta} \right) \right)$, which follows from the use of Hoeffding's inequality [28, 70]. For a relative error ϵ (i.e., absolute error $\|O\|\epsilon$), the sample complexity is simply $\mathcal{O} \left(\frac{1}{\epsilon^2} \log \left(\frac{1}{\delta} \right) \right)$. \square

Appendix F: Resource estimates for the advection equation and nonlinear scalar hyperbolic PDE.

Here, we explicitly provide the empirical estimates of resources used to simulate PDEs in the main text. For the advection equation in Section IV, the resource estimates are presented below.

Encoding/embedding	N	8	16	32	64	128	256
Standard binary (Pauli basis)	2436552	26297612	218866288	1578432842	10836348028	70499518052	
Standard binary (Bell basis)	763908	7458924	43759424	225588544	1012550952	4414678912	
One-hot	639484	1744244	4769716	13250180	36951880	103520984	
Unary	10125952	40444376	130567302	366006134	1022829818	2857164016	

TABLE I. Circuit depths for simulating the linear advection equation (14) with N grid points per dimension.

Encoding/embedding	N	8	16	32	64	128	256
Standard binary (Pauli basis)	2629832	28275344	234049044	1687121012	11502332116	74721198352	
Standard binary (Bell basis)	767438	7605024	44760384	229395044	1027650880	4466948512	
One-hot	2825728	15414848	84305536	468399872	2612538112	14638120448	
Unary	11014808	57868288	312940628	1736912548	9658783388	53824469152	

TABLE II. Two-qubit gates for simulating the linear advection equation (14) with N grid points per dimension.

For the nonlinear scalar hyperbolic PDE in Section V, the resource estimates are presented below.

Encoding/embedding	N_q	8	16	32	64	128	256
Standard binary (Pauli)	3438	10058	25149	56791	111434	173254	
One-hot	448	896	1792	3584	7168	14336	
Unary	900	1348	2244	4036	7620	14788	

TABLE III. Circuit depths for simulating the nonlinear scalar hyperbolic PDE (18) with N_q grid points for q .

Encoding/embedding	N_q	8	16	32	64	128	256
Standard binary (Pauli)	4030	12023	29496	66265	127828	196039	
One-hot	4144	4816	6160	8848	14224	24976	
Unary	5132	5804	7148	9836	15212	25964	

TABLE IV. Two-qubit gates for simulating the nonlinear scalar hyperbolic PDE (18) with N_q grid points for q .

Appendix G: Comparison between Schrödingerization and LCHS

We provide a comparison between Schrödingerization and LCHS when used to simulate non-Hermitian dynamics. As a simple example, we consider the simulation of the transverse-field Ising model (TFIM) with an imaginary longitudinal field:

$$A = -iH = -\gamma_z \sum_{j=1}^n (I - Z_j) - i \left(J \sum_{j=1}^{n-1} Z_j Z_{j+1} + h \sum_{j=1}^n X_j \right). \quad (\text{G1})$$

For Schrödingerization, we consider $N_{\text{S,shots}}$ shots per circuit, where $N_{\text{S,shots}} \in \{10^2, 10^3, 10^4, 10^5\}$. The hybrid LCHS algorithm [28] involves Monte Carlo sampling which induces sampling error in addition to shot noise. Here, we consider the combined standard error due to both sources of randomness. In our simulation, we consider $N_{\text{LCHS,samples}}$ randomly sampled circuits and $N_{\text{LCHS,shots}}$ shots per circuit for a total of $N_{\text{LCHS,samples}} \cdot N_{\text{LCHS,shots}}$ circuit executions. We set $N_{\text{LCHS,samples}} = 100$ and choose $N_{\text{LCHS,shots}}$ such that the total number of circuit executions are the same between Schrödingerization and LCHS. For both methods, we apply the second-order Trotter formula with 20 Trotter steps. In Fig. 7, we plot the estimated value of $\langle O \rangle = \sum_{j=1}^n \frac{I - Z_j}{2}$ obtained by both methods. We find that both methods obtain similar standard error when using the same total number of circuit executions.

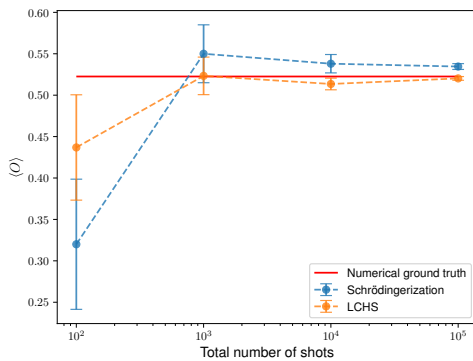


FIG. 7. Estimate of $\langle O \rangle$ at $t = 0.5$ with parameters $J = h = 1$, $\gamma_z = 0.1$. Error bars denote the standard error. The implementation of Schrödingerization uses $n_p = 7$ ancilla qubits to represent $p \in [-R, R]$, where we set $R = 25$. The implementation of LCHS uses the same choice of R to perform Monte Carlo sampling, where $[-R, R]$ is discretized into 128 grid points.